January 2015

Constrained Optimized Command Shaping for Minimizing Residual Vibration in a Flexible-Joint Robot

Alok Agrawal
Purdue University

Graduate School Form 30
(Revised 08/14)

PURDUE UNIVERSITY
GRADUATE SCHOOL
Thesis/Dissertation Acceptance

This is to certify that the thesis/dissertation prepared

By Alok Agrawal

Entitled
Constrained Optimized Command Shaping for Minimizing Residual Vibration in a Flexible-Joint Robot

For the degree of Master of Science in Mechanical Engineering

Is approved by the final examining committee:

Peter H. Meckl

Kartik Ariyur

George Chiu

To the best of my knowledge and as understood by the student in the Thesis/Dissertation Agreement, Publication Delay, and Certification/Disclaimer (Graduate School Form 32), this thesis/dissertation adheres to the provisions of Purdue University's "Policy on Integrity in Research" and the use of copyrighted material.

Peter H. Meckl

Approved by Major Professor(s): _____

_____

Approved by: Anil Bajaj/JDJ 07/08/2015

Head of the Department Graduate Program Date

CONSTRAINED OPTIMIZED COMMAND SHAPING FOR MINIMIZING RESIDUAL VIBRATION IN A FLEXIBLE-JOINT ROBOT

A Thesis

Submitted to the Faculty

of

Purdue University

by

Alok Agrawal

In Partial Fulfillment of the

Requirements for the Degree

of

Master of Science in Mechanical Engineering

August 2015

Purdue University

West Lafayette, Indiana

ACKNOWLEDGMENTS

I extend my most sincere gratitude to my thesis advisor, Peter Meckl, for his invaluable inputs throughout this research and his patience in guiding me whenever I faced obstacles. I wish to thank my parents for their unsolicited support and encouragement that helped me stay motivated and focused. I wish to thank other members of my advisory committee, George Chiu, Bin yao and Kartik Ariyur for their willingness and time to serve in this capacity. I would also like to thank my research partner Yumeng, for his great help in tuning up the experimental setup and long hours spent in conducting experiments runs. I want to give special thanks to my lab partner, Jay, for his willingness in exchanging ideas and discussing concepts that often helped me find new solutions. I am also grateful to the members of the Ruth and Joel Spira Laboratory for Electromechanical Systems and the staff at the mechanical engineering e-shop for their willingness in listening to my problems and their suggestions in troubleshooting multiple hardware issues.

TABLE OF CONTENTS

LIST OF TABLES

LIST OF FIGURES

Figure Page

ABSTRACT

Agrawal, Alok. MSME, Purdue University, August 2015. Constrained Optimized Command Shaping for Minimizing Residual Vibration in a Flexible-Joint Robot. Major Professor: Peter H. Meckl, School of Mechanical Engineering.

Joint flexibility is a natural trait of robotic manipulators, which limits fast point-to-point motion. Remedial measures are often employed to enable these systems to perform their goal in a desired manner. These measures range from either modifying the system dynamics such that the resonance is increasingly damped or by designing cleverly shaped input commands that avoid exciting the resonant modes altogether. In this work, a numerical framework for generating constrained shaped commands for a two-link flexible-joint robot is presented. To optimally select the design parameters for generating shaped commands, the effects of subjecting the optimization to mutually exhaustive constraints of residual vibration performance, speed of motion and size of actuators has been studied. Few important performance metrics to characterize the performance are also introduced and discussed. The framework has been tested for two basis functions, ramped sinusoid and segmented versine, in simulations and experiments and performance is evaluated against one another and an unshaped bang-bang profile. In practice, it has been shown that the constrained numerical approach reduces vibration in the nonlinear robot system in a more effective and efficient manner than the unconstrained closed-form solution.

1. INTRODUCTION

1.1 Motivation

Modern computer-controlled engineering systems are designed to execute fast point-to-point motion. Such systems include industrial manipulators, high speed disk drive heads, chip manufacturing systems, flexible space structures, etc. For these systems, flexibility is a natural characteristic and can be both detrimental and necessary at times. Commonly, every mechanical system has some joint flexibility which could occur from transmission elements like gears, belt drives, actuators or even measurement devices like a rotary torque sensor [1]. In certain cases, joint flexibility is intentionally built into the design for environments where there is a human machine interaction. Flexibility could help reduce collision impact and damage in case of an accident.

Typically, robot manipulators, in various application settings ranging from manufacturing automobile parts to flipping muffins, are required to track trajectories to perform pick and place operations. These operations are desired to be performed as fast and as accurately as possible. With conflicting performance requirements, any effort to move the system quickly would excite large vibrations due to rapid repositioning and high acceleration forces and, as such, resonance due to flexibility is always a limiting factor for precise motion control. Especially in underdamped sys-

tems, residual vibrations may increase the settling times and bring down the overall productivity.

1.2 Literature Review

Standard feedback methods could be used to alleviate the problem to an extent but the overall closed loop damping could still be insufficient to improve on the vibration problem effectively. References [2] and [3] have proven the necessity to consider joint flexibility to achieve desired control performance. There are two common approaches to the precise motion control of mechanical systems with joint flexibility. The first one aims to modify the system dynamics such that the system responds appropriately to the input by incorporating feedback control, and the second approach modifies the input itself through feedforward control. In the first approach, an attempt is made to control the system through vibration by forcing it to follow whatever trajectory is input. In the literature on flexible joint mechanical systems, researchers have examined multiple standard feedback control methods. One example of using a simple PD loop feedback for control of flexible systems is shown by Tomie in [4]. More involved robust and adaptive control methods have also been researched for similar systems, [5]. A good discussion on various control techniques for flexible joint robots can be found in [1].

The control paradigms for flexible dynamic systems could broadly be classified into two categories. The first involves controlling the end-effector position directly by modeling the flexible modes and using link position in the control loop. However,

controlling the system through the flexible elements is difficult and has a limited bandwidth. It also frequently encounters problems with actuator saturation in providing more control effort to track the desired end-point trajectory through vibrations. The second category involves controllers that act only on actuators and do not involve complete robot dynamics, especially the modeling of flexible modes. These controllers are simpler and make use of feedforward control that manipulates the input to the system. The feedforward compensation uses clever command generation techniques to reduce residual vibrations satisfactorily.

Feedforward techniques can further be divided into two categories, inverse and forward compensation. In inverse compensation, first the reference input is designed, and corresponding to that input, using the inverse dynamics model of the system, the related input force is calculated, [6]. The chief drawback of the inverse dynamics method is the instability of plant inverse for non-minimum phase systems. This shortcoming can be handled by using pseudo-inverse methods, [7] or by applying more sophisticated inverse adaptive feedforward control where the output error is used to modify the weights of a compensator, such as a neural network, [8]. Also, these techniques are usually conservative and achieve vibration performance at the expense of longer move times.

In forward compensation, a force applied to the system is constructed first and then the reference trajectories that produce that force are derived. The command shaping technique falls under the umbrella of such forward compensation. Input shaping or command shaping techniques aim to design inputs that avoid excitation of

flexible modes. One of the simplest command shaping methods attempts to reduce the sharpness of transitions in an input to remove all the high frequency components that could cause resonance in the flexible joint. The smoothness of transitions is governed by the desired bandwidth, which is kept below the lowest natural frequency of the system, [9]. This method is easy to implement as it requires no information about the system flexibility but slewing the large frequency band results in appreciably longer move times.

Over the years various command generation methods have been proposed. One of the early forms of command shaping, called posicast control was developed by Smith in the 1950s [10]. It proposed a basic wave cancellation technique to remove vibrations in underdamped systems. This method, unfortunately, was susceptible to modeling errors in natural frequency and damping. In another systematic approach, the knowledge of natural frequencies of the system is utilized in a manner such that the critical frequency content in the inputs at the spectral location of flexible modes is reduced. In [11], Singer and Seering proposed an input shaping technique that convolves a general input command with a finite impulse response (FIR) filter to remove energy at the system resonant frequencies. In [12], Bhat and Miu showed that filtering in effect has the Laplace domain equivalence of placing zeros at undesirable system poles. This is useful in the way that if we don't have any control on the type of input at the disposal of the system, suitable FIR filters which are designed specifically for the flexible modes in the system, can be convolved with the input to reduce the vibration. However, one might naturally question what kind of performance

refinements can be achieved if we had more control of the design or constraints of the input.

One such approach to synthesize shaped commands is through the use of harmonics of appropriately selected basis functions. The harmonics can be used to construct a desired command that minimizes energy content at the points of system natural frequency. This approach was proposed by Meckl in [13], [14] and has been applied in this study. In [15], a detailed comparison of the two shaping methods has been discussed and relative merits of each paradigm have been experimentally demonstrated. Roover and sperling, [16], have also presented a good general discussion on shaping techniques in reference to feedback and feedforward compensation for vibration reduction. The command shaping approach is robust to modeling errors and has progressed in a way that it has proven to be effective for multimode systems [17], time-varying systems [18] and systems with configuration-dependent resonance [19].

1.3 Overview of Thesis

In this research, the command shaping approach from [14] and [20] has been adopted in application to a two-link flexible-joint robot. The command shaping approach derives time optimality from a least square approximation of a bang-bang, i.e., square wave profile, through a set of basis functions [13]. With least squares fit, similar to an approximation with Fourier series, at every jump discontinuity, ringing effects are observed. This ringing, also called Gibbs phenomenon, eventually results in shaped profiles demanding high intermittent peak torques. Therefore, in this work a

numerical optimization framework is developed which allows smoother approximation to the bang-bang function by adding constraints in the design of the shaped inputs. A tradeoff between time optimality and vibration performance has been investigated in light of peak acceleration or torque demands on the actuators. Tests have been conducted in simulation and experiment and a comparative analysis of relative merits and drawbacks of the constrained optimization against earlier closed-form approach has been presented. The command inputs used in this work are unshaped bang-bang profile, ramped sinusoid and segmented versine.

An important consideration in multimode, multi-link systems is defining a performance metric to quantify vibration performance. To address this, different key measures of residual vibration have been critically evaluated. These methods have been mathematically classified and qualitative implications are drawn. This paper is organized as follows. First, a physical and mathematical understanding of the two-link flexible joint robot setup is presented in Chapter 2. In Chapter 3, a solution to Gibbs phenomenon for the chosen basis functions and an outline for constrained optimization method is presented. It then discusses the validation of proposed approach and shaping parameter consideration through design simulations. Experimental evaluation of the shaped profiles and discussion on performance metrics is presented in Chapter 4. Lastly, Chapter 5 draws important inferences and summarizes contributions of this research.

2. ROBOT MODEL AND SYSTEM DESCRIPTION

To generate suitable commands and study their application on the robot, it is first necessary to gain a good understanding of the system. Sections 2.1 and 2.2 of this chapter talk about the two-link robot and the mathematical models that are used for controller design, simulation and implementation of the shaped commands. Two variants of the mathematical model are included. The first one is the complete Lagrangian model used for precise simulations and, to facilitate control design, a reduced model is also presented. In 2.3, a description of important system parameters, their definition and estimated values is presented. The next section details the controller design in place followed by a discussion of configuration-dependent resonance in the manipulator system.

2.1 The Two-Link Robot

The custom-built two-link robot is setup at Ruth and Joel Spira Laboratory for Electromechanical Systems in the School of Mechanical Engineering at Purdue University. As shown in Figure 2.1, the robot is designed to operate in a horizontal plane and can be basically thought of as a two-link serial manipulator. The two links are interchangeably referred to as link 1 and link 2 or shoulder link and elbow link. The robot was designed by [21] as a rigid-joint serial manipulator and was later modi-

fied by Kinceler to include compliance by adding flexible joints in [22]. The links are driven by two electric brushless DC motors. In [23], Chatlatanagulchai set the robot controller with LabVIEW data acquisition environment and programmed the FPGA. More details on technical specifications of driving elements and sensors in the hardware are included in chapter 4. The robot base mounts the first motor and the encoder, providing an inertial frame of reference to the driven shoulder link. The shoulder link houses the second motor, which drives the elbow link. Each motor drives the corresponding link through a belt drive with a gear ratio of 5. Joint compliance is introduced by adding torsional springs between the sprocket driven by the motor and the link. As such, the motors only act on the torsional springs but not on the link directly. The two torsional springs included in the robot have spring coefficients ranging from 10^3 to 10^5Nm/rad, which are, by design, rather low compared to joint compliance in standard industrial manipulators [1]. Thus, the robot proves to be a challenging test bed for investigating control and trajectory design methods.

2.2 Mathematical Robot Model

Notation of all the physical model parameters can be visualized in Figure 2.2. The models presented in the following subsections are utilized in numerical simulation, control law design and calculation of system natural frequencies. It is important to note that shoulder link and motor angles, θ_1 and θ_3, are defined and measured in an inertial frame, whereas elbow link and motor angles, θ_2 and θ_4, are defined and measured relative to shoulder link position, θ_1.

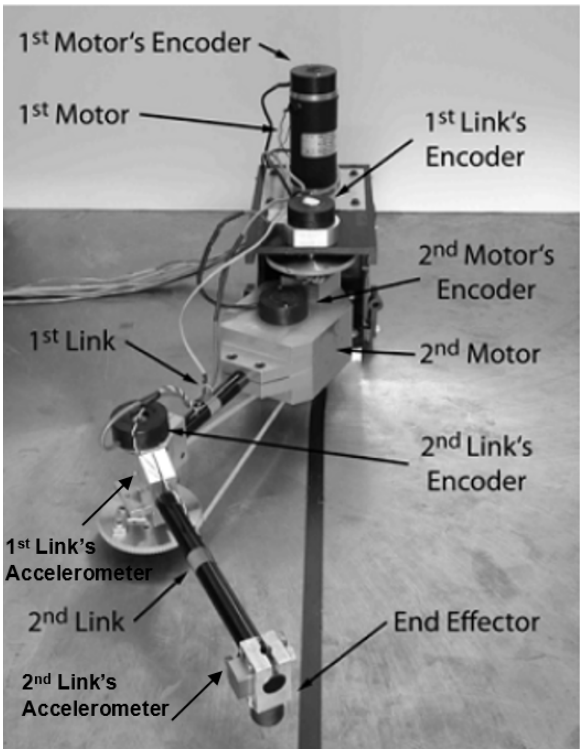

Figure 2.1. The two-link flexible-joint robot.

2.2.1 Lagrangian Model

A Lagrangian model of the robot was derived by Nho in [24] incorporating coulomb and viscous friction in the motor bearings and links as well as viscous damping in the joints due to linear torsional springs. This model originally included a payload mass in the dynamics. For the focus of the present study, the effect of payload mass is not considered and hence it is omitted in simulations and experimental analysis.

For the system setup as shown in Figure 2.2, the Lagrangian model can be stated as

$$\mathbf{M}(\theta)\ddot{\theta} + \mathbf{V}(\theta, \dot{\theta}) + \mathbf{C}\dot{\theta} + \mathbf{K}\theta + \mathbf{D} = \mathbf{T} \tag{2.1}$$

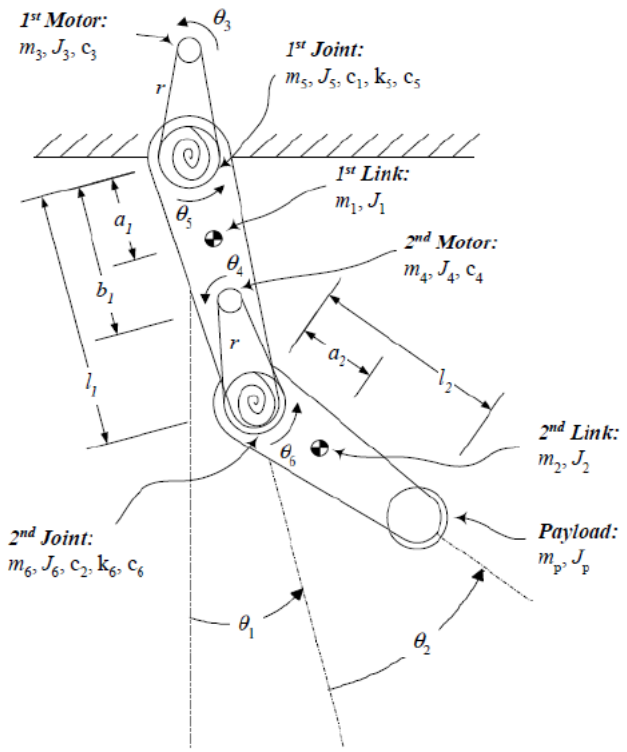

Figure 2.2. Schematic of the robot with physical parameters, [24].

where θ is the generalized coordinate vector $\theta_{\mathbf{i}}$, $\mathbf{M}(\theta)$ denotes the inertia matrix, $\mathbf{V}(\theta, \dot{\theta})$ denotes the vector of Coriolis and centrifugal functions, $\mathbf{C}$ is the viscous damping matrix, $\mathbf{K}$ is the stiffness coefficient matrix, $\mathbf{D}$ is the Coulomb friction vector, and $\mathbf{T}$ represents the torque vector from the driving motors. It is to be noted that the comparatively fast dynamics of the servo amplifiers is not taken into account and the motors are considered to be ideal torque sources.

The inertia matrix $\mathbf{M}(\theta)$ is written as

$$\mathbf{M}(\theta) = \begin{bmatrix} \mathbf{M_1}(\theta_2) & \mathbf{M_2} \\ \mathbf{M_2^T} & \mathbf{M_3} \end{bmatrix}, \tag{2.2}$$

where

$$\mathbf{M_1}(\theta_\mathbf{2}) = \begin{bmatrix} m_{11} & m_{12} \\ m_{21} & m_{22} \end{bmatrix}, \tag{2.3}$$

$$\mathbf{M_2} = \begin{bmatrix} 0 & m_{41} \\ 0 & 0 \end{bmatrix}, \tag{2.4}$$

$$\mathbf{M_3} = \begin{bmatrix} m_{33} & 0 \\ 0 & m_{44} \end{bmatrix}, \tag{2.5}$$

The matrix elements are given as

$$m_{11} = m_1 a_1^2 + m_2(l_1^2 + a_2^2) + m_4 b_1^2 + m_6 l_1^2$$
$$+J_1 + J_2 + J_4 + J_6 + 2l_1 m_2 a_2 cos(\theta_2), \tag{2.6}$$

$$m_{12} = m_{21} = m_2 a_2^2 + J_2 + l_1 m_2 a_2 cos(\theta_2), \tag{2.7}$$

$$m_{14} = J_4 + \frac{J_6}{r}, \tag{2.8}$$

$$m_{22} = m_2 a_2^2 + J_2, \tag{2.9}$$

$$m_{33} = J_3 + \frac{J_5}{r^2}, \tag{2.10}$$

and

$$m_{44} = J_4 + \frac{J_6}{r^2}, \tag{2.11}$$

where m_i refers to the lumped masses, J_i to the moments of inertia, l_i to the link lengths, and a_1, a_2 represent the distances of the center of gravity of link 1 and link 2 from their respective first and second joints. The distance between the second motor and the first joint is denoted by b_1, and r denotes the chain drive gear ratio.

The Coriolis and centrifugal functions vector is calculated as

$$\mathbf{V}(\theta,\dot{\theta}) = \begin{bmatrix} V_L \\ 0 \end{bmatrix} = \begin{bmatrix} -l_1 m_2 a_2 (2\dot{\theta_1}\dot{\theta_2} + \dot{\theta_2^2}) sin(\theta_2) \\ l_1 m_2 a_2 \dot{\theta_1^2} sin(\theta_2) \\ 0 \\ 0 \end{bmatrix}, \tag{2.12}$$

and the viscous damping matrix can be written as

$$\mathbf{C} = \begin{bmatrix} c_1 + c_5 & 0 & \frac{-c_5}{r} & 0 \\ 0 & c_2 + c_6 & 0 & \frac{-c_6}{r} \\ \frac{-c_5}{r} & 0 & c_3 + \frac{-c_6}{r^2} & 0 \\ 0 & \frac{-c_6}{r} & 0 & c_4 + \frac{c_6}{r^2} \end{bmatrix}, \tag{2.13}$$

where c_i represents the viscous friction coefficients.

The stiffness coefficients of the springs are combined to denote the matrix of stiffness coefficients as

$$\mathbf{K} = \begin{bmatrix} k_5 & 0 & \frac{-k_5}{r} & 0 \\ 0 & k_6 & 0 & \frac{-k_6}{r} \\ \frac{-k_5}{r} & 0 & \frac{-k_5}{r^2} & 0 \\ 0 & \frac{-k_6}{r} & 0 & \frac{k_6}{r^2} \end{bmatrix}, \tag{2.14}$$

where k_i represents the torsional springs' coefficients.

The Coulomb friction vector is written as

$$\mathbf{D} = \begin{bmatrix} D_L \\ D_M \end{bmatrix} = \begin{bmatrix} -d_1 sign(\dot{\theta_1}) \\ -d_2 sign(\dot{\theta_2}) \\ -d_3 sign(\dot{\theta_3}) \\ -d_4 sign(\dot{\theta_4}) \end{bmatrix}, \tag{2.15}$$

and lastly, the torque vector is obtained as

$$\mathbf{T} = \begin{bmatrix} 0 \\ T_M \end{bmatrix} = \begin{bmatrix} 0 \\ 0 \\ T_1 \\ T_2 \end{bmatrix}, \tag{2.16}$$

wherein T_1 and T_2 represent the driving torque for the first and second motor.

2.2.2 Simplified Model

The full Lagrangian dynamics model is a relatively complex model which makes design of model-based feedback controllers rather difficult. Hence, it is useful to write out a simplified model that still retains the important characteristics of the dynamic behavior. A widely accepted reduced model in the literature was introduced by Spong in [25]. This reduced model can be derived from the full model by considering two important assumptions. First, the damping of torsional springs, c_5 and c_6, is justly

neglected because of typically smaller magnitudes of damping coefficients. Thus, the viscous damping matrix Equation (2.13) is reduced to

$$\mathbf{c_{red}} = \begin{bmatrix} \mathbf{C_L} & 0 \\ 0 & \mathbf{C_M} \end{bmatrix}, \tag{2.17}$$

The resulting diagonal elements simplify to the link damping matrix and the motor damping matrix, respectively.

$$\mathbf{C_L} = diag\{c_1, c_2\}, \mathbf{C_M} = diag\{c_3, c_4\} \tag{2.18}$$

Based on Equation (2.17), the robot model can be rewritten for the links as

$$\mathbf{M_1}(\theta_\mathbf{L})\ddot{\theta_\mathbf{L}} + \mathbf{M_2}\ddot{\theta_\mathbf{M}} + \mathbf{V_L}(\theta_\mathbf{L}, \dot{\theta_\mathbf{L}}) + \mathbf{C_L}\dot{\theta_\mathbf{L}} + \mathbf{K_S}(\theta_\mathbf{L} - \frac{\theta_\mathbf{M}}{\mathbf{r}}) = \mathbf{0} \tag{2.19}$$

and that for the motors as

$$\mathbf{M_2^T M_3}\ddot{\theta_\mathbf{M}} + \mathbf{C_M}\dot{\theta_\mathbf{M}} + \mathbf{K_S}(\frac{\theta_\mathbf{M}}{\mathbf{r^2}} - \frac{\theta_\mathbf{L}}{\mathbf{r}}) = \mathbf{T_M} \tag{2.20}$$

where

$$\mathbf{K_S} = diag\{k_5, k_6\} \tag{2.21}$$

Spong's reduced model makes a second assumption that the kinetic energy of the motors is mainly due to their own rotation, which gives

$$\mathbf{M_{red}}(\theta)\ddot{\theta} + \mathbf{V}(\theta, \dot{\theta}) + \mathbf{C_{red}}\dot{\theta} + \mathbf{K}\theta = \mathbf{T} \tag{2.22}$$

where

$$\mathbf{M_{red}}(\theta) = \begin{bmatrix} \mathbf{M_1}(\theta_\mathbf{L}) & 0 \\ 0 & \mathbf{M_3} \end{bmatrix}, \tag{2.23}$$

is the reduced inertia matrix which differs from Equation (2.2) in the zero non-diagonal elements $\mathbf{M_2}$. This assumption is predicated on the fact that for larger drive ratios, $\mathbf{r} >> 1$, the rotor angular velocity for the motor will be much larger than the link angular velocity and, therefore, the non-diagonal term $\mathbf{M_2}$ can be safely neglected. Now, the dynamics equations for links and the motors can be respectively written as

$$\mathbf{M_1}(\theta_\mathbf{L})\ddot{\theta_\mathbf{L}} + \mathbf{V_L}(\theta_\mathbf{L}, \dot{\theta_\mathbf{L}}) + \mathbf{C_L}\dot{\theta_\mathbf{L}} + \mathbf{K_S}(\theta_\mathbf{L} - \frac{\theta_\mathbf{M}}{\mathbf{r}}) = \mathbf{0} \tag{2.24}$$

for the links and

$$\mathbf{M_3}\ddot{\theta_\mathbf{M}} + \mathbf{C_M}\dot{\theta_\mathbf{M}} + \mathbf{K_S}(\frac{\theta_\mathbf{M}}{\mathbf{r^2}} - \frac{\theta_\mathbf{L}}{\mathbf{r}}) = \mathbf{T_M} \tag{2.25}$$

for the motors. It can be clearly noted that the motors and the links are only coupled by torsional springs in the joints. With state variable x being defined as

$$\mathbf{x} = \begin{bmatrix} \theta_L \\ \theta_M \\ \dot{\theta_L} \\ \dot{\theta_M} \end{bmatrix}, \tag{2.26}$$

Equations (2.24) and (2.25) can now be expressed as a 4^{th} order state space system as

$$\begin{aligned} \dot{\mathbf{x_1}} &= \mathbf{x_3}, \\ \dot{\mathbf{x_2}} &= \mathbf{x_4} \\ \dot{\mathbf{x_3}} &= -\mathbf{M_1}^{-1}[\mathbf{V_L} + \mathbf{C_L}\dot{\theta_\mathbf{L}} + \mathbf{K_S}(\theta_\mathbf{L} - \frac{\theta_\mathbf{M}}{\mathbf{r}})] \\ \dot{\mathbf{x_4}} &= -\mathbf{M_3}^{-1}[\mathbf{T_M} - \mathbf{C_M}\dot{\theta_\mathbf{M}} - \mathbf{K_S}(\frac{\theta_\mathbf{M}}{\mathbf{r^2}} - \frac{\theta_\mathbf{L}}{\mathbf{r}})] \end{aligned} \tag{2.27}$$

Here the arguments have been removed for brevity.

2.3 System Parameters

Precise knowledge of the robot's physical parameters is necessary for generating command inputs, designing model-based controllers and developing a good simulation model. Especially in light of nonlinearities and deformities that overstep modeling assumptions, system identification of the robot poses an interesting problem. Over the years, various approaches have been chosen to make parameter estimations through measurements and experiments. In [24], Nho performed first system identification for the two-link robot through a least squares approach, where certain parameter groups were formed to simplify and linearize the Lagrangian model. Doing so, all the parameters of the robot were simultaneously determined. In Nho's approach, all the experiments performed were open-loop. Lee, in [26], first re-performed the estimation routine using closed-loop experiments. Later, Lee introduced a new parameter estimation approach based on Fourier regularization. This method led to better estimates but offsets in torque still remained in the simulation model. In [27], Scheel developed a new method to identify the robot parameters by splitting the identification process into smaller parts. The identification process was divided into: 1) the motors 2) the second link and 3) the first link. The estimated values in this procedure were able to capture the important dynamic behavior of the robot very well and have been used in this work. Table 2.1 lists the physical values of the robot's parameters. Here p_1, p_2 and p_3 are written from Equation (2.37) as:

Table 2.1. Identified physical values of the robot's parameters. [27]

Parameter	**Value**	**Parameter**	**Value**
p_1	$0.140 \frac{\text{kg m}^2}{\text{rad}}$	c_4	$1.497 \cdot 10^{-3} \frac{\text{Nms}}{\text{rad}}$
p_2	$0.0196 \frac{\text{kg m}^2}{\text{rad}}$	c_5	$0.005 \frac{\text{Nms}}{\text{rad}}$
p_3	$0.0234 \frac{\text{kg m}^2}{\text{rad}}$	c_6	$8.128 \cdot 10^{-5} \frac{\text{Nms}}{\text{rad}}$
J_3	$4.157 \cdot 10^{-5} \frac{\text{kg m}^2}{\text{rad}}$	k_5	$2.848 \frac{\text{Nm}}{\text{rad}}$
J_4	$7.543 \cdot 10^{-4} \frac{\text{kg m}^2}{\text{rad}}$	k_6	$2.848 \frac{\text{Nm}}{\text{rad}}$
J_5	$0.025 \frac{\text{kg m}^2}{\text{rad}}$	d_1	0.0199 Nm
J_6	$0.025 \frac{\text{kg m}^2}{\text{rad}}$	d_2	0.0323 Nm
c_1	$0.04 \frac{\text{Nms}}{\text{rad}}$	d_3	0.0053 Nm
c_2	$0.0214 \frac{\text{Nms}}{\text{rad}}$	d_4	0.0271 Nm
c_3	$1.894 \cdot 10^{-4} \frac{\text{Nms}}{\text{rad}}$		

$$p_1 = m_1 a_1^2 + m_2 l_1^2 + m_4 b_1^2 + m_6 l_1^2 + J_1 + J_4 + J_6, \tag{2.28}$$

$$p_2 = m_2 a_2^2 + J_2, \tag{2.29}$$

and

$$p_3 = l_1 m_2 a_2. \tag{2.30}$$

2.4 Computed Torque Controller

Through the years, many robot control schemes have been proposed in the literature, ranging from adaptive control, robust control, learning control and so on, [28]. In this work, to ensure motor trajectory tracking, external disturbance rejection and handling modeling uncertainties, a computed torque controller is applied in a similar manner as [19]. Computed torque controller is a special case of *feedback linearization* form of nonlinear controllers. It uses estimates from a model of the robot to cancel out nonlinear behavior and reduces nonlinear dynamics to decoupled linear error equations.

Computed torque uses control law partitioning and is divided into a servo-based part and a model-based part. The model-based part works to reduce the nonlinear behavior of the motors, while the servo-based portion ensures asymptotic tracking of the input trajectories. The servo-based part is simply a PD feedback controller that compensates any disturbances or modeling errors. Since the cross-coupling terms are

negligible in Equation (2.2), the model-based part uses a mix of complete Lagrangian model and the reduced model, with inertia matrix in Equation (2.2) replaced by Equation (2.23). This is a reasonable assumption and it permits much simpler implementation of the controller. Let $\mathbf{C_H}$ represent the bottom two rows of the viscous damping matrix in Equation (2.13) and $\mathbf{K_S} = \text{diag}\,(k_5, k_6)$ represent the diagonal matrix consisting of spring coefficients. Also, if $\boldsymbol{\theta_L}$ and $\boldsymbol{\theta_M}$ denote the link and motor positions, respectively, we can write the model-based part as:

$$\mathbf{T_{mb}} = \mathbf{C_H}\dot{\boldsymbol{\theta}} + \mathbf{D_M} + \mathbf{K_S}\left(\frac{\boldsymbol{\theta}_\mathbf{M}}{r^2} - \frac{\boldsymbol{\theta}_\mathbf{L}}{r}\right) \tag{2.31}$$

and the servo-based part as

$$\mathbf{T_{sb}} = \mathbf{M_3}\Big(\ddot{\boldsymbol{\theta}}_{\mathbf{M,d}} + \mathbf{K_v}\left(\dot{\boldsymbol{\theta}}_{\mathbf{M,d}} - \dot{\boldsymbol{\theta}}_\mathbf{M}\right) + \mathbf{K_p}\left(\boldsymbol{\theta}_{\mathbf{M,d}} - \boldsymbol{\theta}_\mathbf{M}\right)\Big), \tag{2.32}$$

with index d in Equation (2.32) representing the desired values of motor acceleration, velocity and the position in the input trajectory. $\mathbf{K_p}$ and $\mathbf{K_v}$ denote the diagonal matrices for proportional and derivative gains for each motor joint, respectively. Therefore, net torque to the robot is:

$$\mathbf{T_{CT}} = \mathbf{T_{mb}} + \mathbf{T_{sb}}. \tag{2.33}$$

Application of computed torque, Equation (2.33), along with the described robot model, Equation (2.1), gives the following closed-loop motor tracking error dynamics,

$$\ddot{\mathbf{e}}_\mathbf{M} + \mathbf{K_v}\dot{\mathbf{e}}_\mathbf{M} + \mathbf{K_p}\mathbf{e_M} = 0. \tag{2.34}$$

where the motor tracking error has been defined as $\mathbf{e_M} = \boldsymbol{\theta}_{\mathbf{M,d}} - \boldsymbol{\theta}_\mathbf{M}$. $\mathbf{K_p}$ and $\mathbf{K_v}$ are chosen such that Equation (2.34) is Hurwitz. Therefore, computed torque ensures

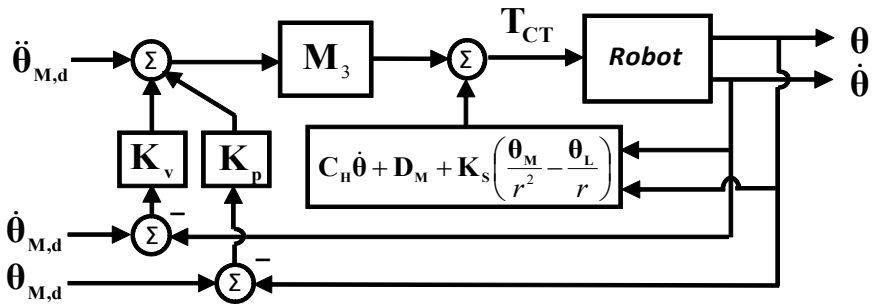

Figure 2.3. Block diagram representation of computed torque controller and the robot, [19].

asymptotic tracking and results in stable internal dynamics for the link subsystem. Figure 2.3 shows a block diagram of the closed-loop system with the controller.

2.5 Configuration-Dependent Resonance

To suitably apply command shaping to the robot, it is necessary to calculate the varying natural frequencies of the robot. This calculation is done by linearization of the combined feedback controller system and the robot loop. The change in frequencies of the robot occur due to varying inertia of the robot manipulator based on the configuration of the two links. The natural frequency for a nonlinear system is usually obtained by linearizing around an equilibrium point. As noted in section 2.2, the inertia matrix in Equation (2.2) is a function of θ_2, the position of the second link and therefore the system resonant frequencies also vary with θ_2.

The closed-loop equations for the robot are obtained by substituting Equation (2.33) into the complete Lagrangian model Equation (2.1). The resulting equations are linearized by performing Taylor expansion of all the rows up to the first-order

term for an equilibrium point of zero velocity and zero acceleration as a function of θ_2. Derivatives of the Coulomb friction terms with respect to the velocities were assumed to be zero and therefore, linear equations don't feature Coulomb friction. The linear closed-loop dynamics can now be given as

$$\mathbf{M_{lin}}\ddot{\theta} + \mathbf{C_{lin}}\dot{\theta} + \mathbf{K_{lin}}\theta = \mathbf{0} \tag{2.35}$$

where the linearized inertia matrix is

$$\mathbf{M_{lin}} = \begin{bmatrix} m_{11,lin} & m_{12,lin} & 0 & m_{14} \\ m_{21,lin} & m_{22} & 0 & 0 \\ 0 & 0 & m_{33} & 0 \\ 0 & 0 & 0 & m_{44} \end{bmatrix}, \tag{2.36}$$

where $m_{11,lin}$, $m_{12,lin}$ and $m_{21,lin}$ are the linearized matrix entities

$$\begin{aligned} m_{11} = {} & m_1 a_1^2 + m_2(l_1^2 + a_2^2) + m_4 b_1^2 + m_6 l_1^2 \\ & + J_1 + J_2 + J_4 + J_6 + 2 l_1 m_2 a_2 cos(\theta_{2,lin}), \end{aligned} \tag{2.37}$$

$$m_{12} = m_{21} = m_2 a_2^2 + J_2 + l_1 m_2 a_2 cos(\theta_{2,lin}), \tag{2.38}$$

Also, the closed-loop viscous damping matrix is given by

$$\mathbf{C_{lin}} = \begin{bmatrix} c_1 + c_5 & 0 & \frac{-c_5}{r} & 0 \\ 0 & c_2 + c_6 & 0 & \frac{-c_6}{r} \\ 0 & 0 & m_{33} K_{v,3} & 0 \\ 0 & 0 & 0 & m_{44} K_{v,4} \end{bmatrix}, \tag{2.39}$$

and the closed loop stiffness matrix is

$$\mathbf{K_{lin}} = \begin{bmatrix} k_5 & 0 & \frac{-k_5}{r} & 0 \\ 0 & k_6 & 0 & \frac{-k_6}{r} \\ 0 & 0 & m_{33}K_{p,3} & 0 \\ 0 & 0 & 0 & m_{44}K_{p,4} \end{bmatrix}, \tag{2.40}$$

Now, for the linearized closed loop dynamic model, the natural frequencies are calculated by determining the imaginary parts of the eigenvalues of the system matrix $\mathbf{A}$ given by

$$\mathbf{A} = \begin{bmatrix} \mathbf{0} & \mathbf{I} \\ -\mathbf{M_{lin}}^{-1}\mathbf{K_{lin}} & -\mathbf{M_{lin}}^{-1}\mathbf{C_{lin}} \end{bmatrix}, \tag{2.41}$$

where $\mathbf{M_{lin}}$ denotes the new inertia matrix, $\mathbf{C_{lin}}$ and $\mathbf{K_{lin}}$ are the closed-loop viscous damping matrix and the closed-loop stiffness matrix, respectively. $\mathbf{I}$ denotes an identity matrix.

It is common knowledge that the system resonant frequencies will change and the resonant peak will flatten out more in the presence of increasing system damping. Meckl, [14], studied the effect of damping and concluded that the system response worsens with more inherent damping when it is not considered in the command shaping routine. Command shaping approach proved successful for lightly-damped systems ($\zeta < 0.3$) and since the two-link robot represents one such lightly-damped system, command shaping has been applied in this study without incorporating damping in the shaping process. The change in both the natural frequencies, ω_1 and ω_2, with θ_2 is illustrated in Figure 2.4.

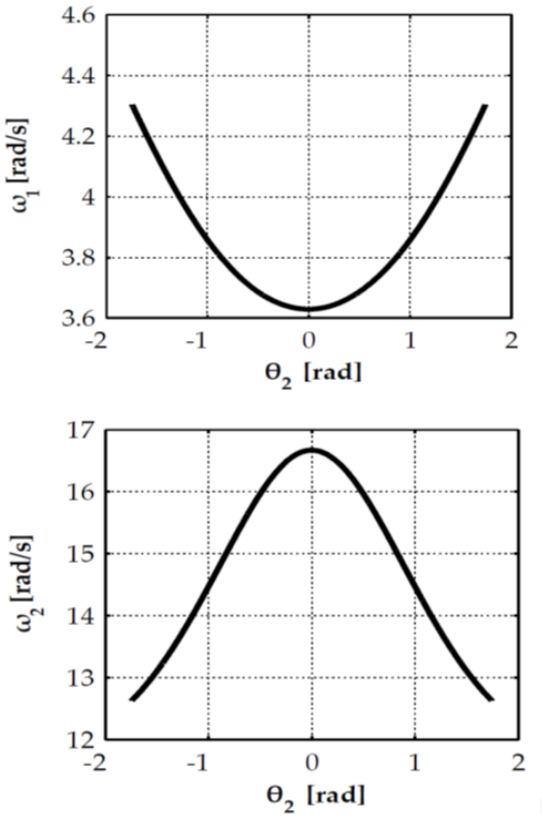

Figure 2.4. Natural frequencies ω_1 and ω_2 as a function of position of the second link θ_2.

3. CONSTRAINED COMMAND SHAPING THROUGH NUMERICAL OPTIMIZATION

This chapter first describes the constructs behind the command shaping approach in section 3.1, (3.1.2) and discusses earlier methods provided in the literature. Then, in 3.2, issues related to Gibbs phenomenon or ringing artifacts in the conventional approach are looked at and their effect on shaping input profiles is studied. In section 3.3, a numerical optimization framework is derived to address the Gibbs effect in reference to command shaping. Implications of the shaped inputs generated using a numerical approach are then studied against the inputs from the original formulation in section 3.4.

3.1 Background

Command shaping removes residual vibrations, essentially by not introducing unwanted energy at the system's natural frequency in the inputs. One of the early works in modifying the frequency content of an input to suppress vibrations was proposed by Aspinwall [29]. A drawback of this method was considerably longer move times than a time optimal bang-bang input. Meckl in [13] introduced a technique to create commands that approximate a bang-bang profile while avoiding resonant energy content. This method involved the use of harmonics of select basis functions

and the troughs in the spectrum depended on the number of employed harmonics. This method was used to design inputs for open-loop controlled systems. Meckl [14] further extended this method to create a weighted, multi-objective fitness function that sought to approximate a square wave and penalize the magnitude of the Fourier transform at critical frequencies in the generated input. Also, a method was proposed to use the commanded signal in conjunction with a feedback controller. In this respect, the controller and plant were treated as one entity and the commanded input served as a reference trajectory to the feedback controller. Beazel, [17], extended the standard command shaping to nonlinear systems with configuration-dependent resonance. In this work, command shaping is adapted in a similar manner, i.e., to generate motor trajectories that effectively suppress vibration in the links.

3.1.1 Theoretical Preliminaries

In [13], Meckl derived an analytical relationship between the residual vibration in a two-mass single-mode system and the Fourier transform magnitude of the forcing function at the flexible mode of the system,

$$A^* = \omega_n T_f \left| F^*(\omega_n T_f) \right|, \tag{3.1}$$

with A^* as the dimensionless residual acceleration amplitude, ω_n as the two-mass system natural frequency, T_f as the move time, and $|F^*(\omega_n T_f)|$ as the dimensionless Fourier transform of the forcing function. It is defined as,

$$|F^*(\omega_n T_f)| = \frac{|F^*(\omega_n)|}{F_{\max} T_f}, \tag{3.2}$$

where $F_{\max}$ is the maximum value of the forcing function. In this study, shaped signals are input to the controller as a reference trajectory and refer to an acceleration profile. In general, the shaped profile is of the form

$$\ddot{\theta}_{rs/v} = \ddot{\theta}_{d,max} f^*(t) = \ddot{\theta}_{d,max} \sum_{l=1}^{L} B_l^* \Phi_l^*(t), \tag{3.3}$$

with $f^*(t)$ being the normalized shaped function ranging between

$$-1 \leq f^*(t) \leq 1, \tag{3.4}$$

and then multiplied by the maximum desired acceleration $\ddot{\theta}_{d,max}$. In $\ddot{\theta}_{rs/v}$, the rs and v stand for Ramped Sinusoid and Versine, which are the two basis functions proposed by Meckl in [13, 14]. More details on the basis functions are provided in section 3.1.2. Therefore, $\ddot{\theta}_{rs/v}$ satisfies $-\ddot{\theta}_{d,max} \leq \ddot{\theta}_{rs} \leq \ddot{\theta}_{d,max}$. $f^*(t)$ consists of a total of L harmonics of the basis function $\Phi^*(t)$ and normalized coefficient B_l^*, where l denotes the l^{th} harmonic $\Phi_l^*(t)$.

The objective function minimizes the residual error between the synthesized command and a bang-bang profile and also the frequency content around the natural frequencies, based on Equation (3.1). Thus, the fitness function for the optimization can be given as,

$$J = \frac{1}{T_f} \left[\int_0^{T_f/2} [1 - f(t)]^2 dt + \int_{T_f/2}^{T_f} [-1 - f(t)]^2 dt \right] + \rho \sum_{i=1}^{11M} (\omega_i T_f)^2 |F^*(\omega_i T_f)|^2, \tag{3.5}$$

where M is the number of resonant frequencies to be attenuated. The parameter ρ is the relative weighting factor between the two objectives. The choice and influence

of this factor is explored in section 3.4. The magnitude of the Fourier transform is reduced in a sufficiently broad range around the natural frequencies by evaluating eleven equally distributed points around each natural frequency in the range of $0.9\omega_n \leq \omega_i \leq 1.1\omega_n$ and providing a tolerance band of $\pm 10\%$ for each frequency. This range and hence the robustness of the method can be adjusted on a case by case basis.

Equation (3.5) is then partially differentiated with respect to all the coefficients, B_l, and the derivatives are then set to zero:

$$\frac{\partial J}{\partial B_r} = 0, \tag{3.6}$$

$r = 1, 2, ..., L$ denotes a particular value of l. The analytical expressions for the ramped sinusoid and versine basis functions can be found in [14]. The coefficients B_l are then normalized so that Equation (3.4) holds:

$$B_l^* = \frac{1}{SF} B_l, \tag{3.7}$$

where SF is the scaling factor, obtained as

$$SF = max[f(t)]. \tag{3.8}$$

3.1.2 Basis Functions

Ramped Sinusoid

The ramped sinusoid basis function was first introduced in [13]. It is given by

$$\Phi_l^*(t) = \frac{1}{\alpha_l}\left(\frac{1}{2} - \tau\right) + \frac{1}{\alpha_l^2}\sin(\alpha_l \tau) - \frac{1}{2\alpha_l}\cos(\alpha_l \tau), \tag{3.9}$$

where τ is the dimensionless time

$$\tau = \frac{t}{T_f}, \tag{3.10}$$

and T_f is the move time of the system and α_l is a characteristic number associated with each harmonic that satisfies the following relation:

$$\alpha_l \sin \alpha_l + 2 \cos \alpha_l - 2 = 0, \tag{3.11}$$

with $\alpha_l \neq n\pi$, where n is an even integer. α_l for the first ten harmonics is listed in Table 3.1. The first three harmonics of the ramped sinusoid are plotted in Figure 3.1.

Table 3.1. Value of α_l for the first ten harmonics of Ramped Sinusoid.

$\mathbf{l^{th}}$**Harmonic**	**Value**
α_1	-8.9688
α_2	-15.4505
α_3	-21.8082
α_4	-28.1324
α_5	-34.4415
α_6	-40.7426
α_7	-47.0389
α_8	-53.3321
α_9	-59.6232
α_{10}	-65.9128

Segmented Versine

In contrast to the ramped sinusoid function that can approximate a full cycle of a square wave consisting of one acceleration and one deceleration phase, the versine function approximates a square pulse. For systems with actuator rate limits, square pulses can be used to drive a system from an initial to a desired velocity state, maintain that state as needed and then take a deceleration phase.

The versine basis function is given by

$$\Phi_l^*(t) = 1 - \cos\left(2\pi l \tau\right), \tag{3.12}$$

where l again denotes the harmonic and is a positive integer.

The segmentation of the versine basis function for command shaping was introduced by Beazel [20]. Nonlinear systems could have natural frequencies that span

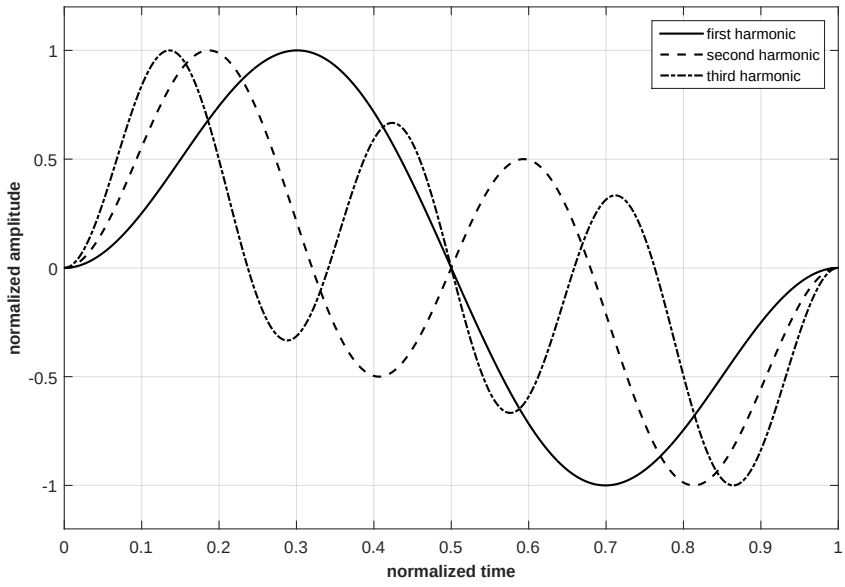

Figure 3.1. First three harmonics of the normalized Ramped Sinusoid function.

over a large band. Efforts to reduce the entire band would be expensive in terms of the longer move times. Thus, Beazel proposed to divide the trajectory into multiple segments and attenuate natural frequency based on linearized operating points for each segment. When the segments are combined, the frequency content of the input signal changes with time and a small band is surgically attenuated in each segment. The first three harmonics of the versine function are plotted in Figure 3.2.

To scale the shaped function and to determine $\ddot{\theta}_{d,max}$, a factor Γ is utilized. It links $\ddot{\theta}_{d,max}$ and $\ddot{\theta}_{B,B}$, the required acceleration to move the system to a desired position with the shaped profile in a specified move time to an equivalent acceleration for a rigid body with bang-bang profile. This relationship and the expressions for Γ depend on the basis function and are given by

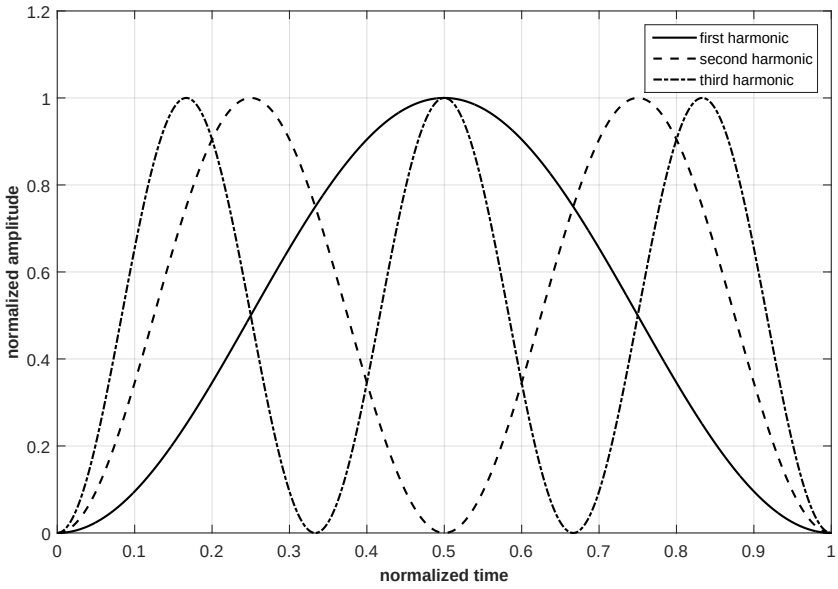

Figure 3.2. First three harmonics of the normalized Versine function.

$$\ddot{\theta}_{d,max,RS} = \ddot{\theta}_{B,B}\Gamma_{RS}^2, \tag{3.13}$$

and

$$\ddot{\theta}_{d,max,V} = \ddot{\theta}_{B,B}\Gamma_V. \tag{3.14}$$

$$\Gamma_{RS} = \sqrt{\frac{3}{\sum_{l=1}^{L} \frac{B_l^*}{\alpha_l}}}, \tag{3.15}$$

and

$$\Gamma_V = \frac{1}{\sum_{l=1}^{L} B_l^*}. \tag{3.16}$$

3.2 Motivation

The first term in Equation (3.5) is a least square approximation of a bang-bang profile, which, simply put, is one cycle of a square wave. The bang-bang solution, where the actuator generates a constant peak force in either the acceleration or deceleration phase, has been proven by mathematicians, [30,31], to be time-optimal for systems in which all their modes are controllable at all times. However, due to the discontinuity at the transition from peak positive to peak negative, the approximation of this function using a finite number of harmonics of a basis function is challenging.

3.2.1 Gibbs Phenomenon

A least square fit to a square wave essentially encounters a problem known as Gibbs phenomenon. Also termed as ringing artifacts, it is the peculiar behavior of

the Fourier series of a piecewise continuous differentiable function f at a jump discontinuity in which the n^{th} partial sum of the Fourier series shows oscillations near the point of the jump. It was first analyzed by Josiah W. Gibbs in 1899, who pointed out that the ringing was a mathematical problem and would always arise during Fourier series synthesis of a discontinuous function. The overshoots and undershoots are the result of approximating a discontinuous function using a finite number of harmonics of continuous basis functions. The partial sum Fourier series approximation using different number of harmonic terms is represented in Figure 3.3.

3.2.2 Mathematical Description of Gibbs Phenomenon

Let f: $\Re \rightarrow \Re$ denote a piecewise continuously differentiable function with a period of $L > 0$. Also, let x_0 be the point of discontinuity with a non-zero gap of a, between the right limit $f(x_0^+)$ and left limit $f(x_0^-)$ of the function f.

$$f(x_0^+) - f(x_0^-) = a \neq 0. \tag{3.17}$$

Let $S_N f$ be the N^{th} partial Fourier series (for each integer $N \geq 1$),

$$\begin{aligned} S_N f(x) :=& \sum_{-N \leq n \leq N} \hat{f}(n) e^{2\pi i n x / L} \\ =& \frac{1}{2} a_0 + \sum_{n=1}^{N} a_n \cos\left(\frac{2\pi n x}{L}\right) + b_n \sin\left(\frac{2\pi n x}{L}\right) \end{aligned} \tag{3.18}$$

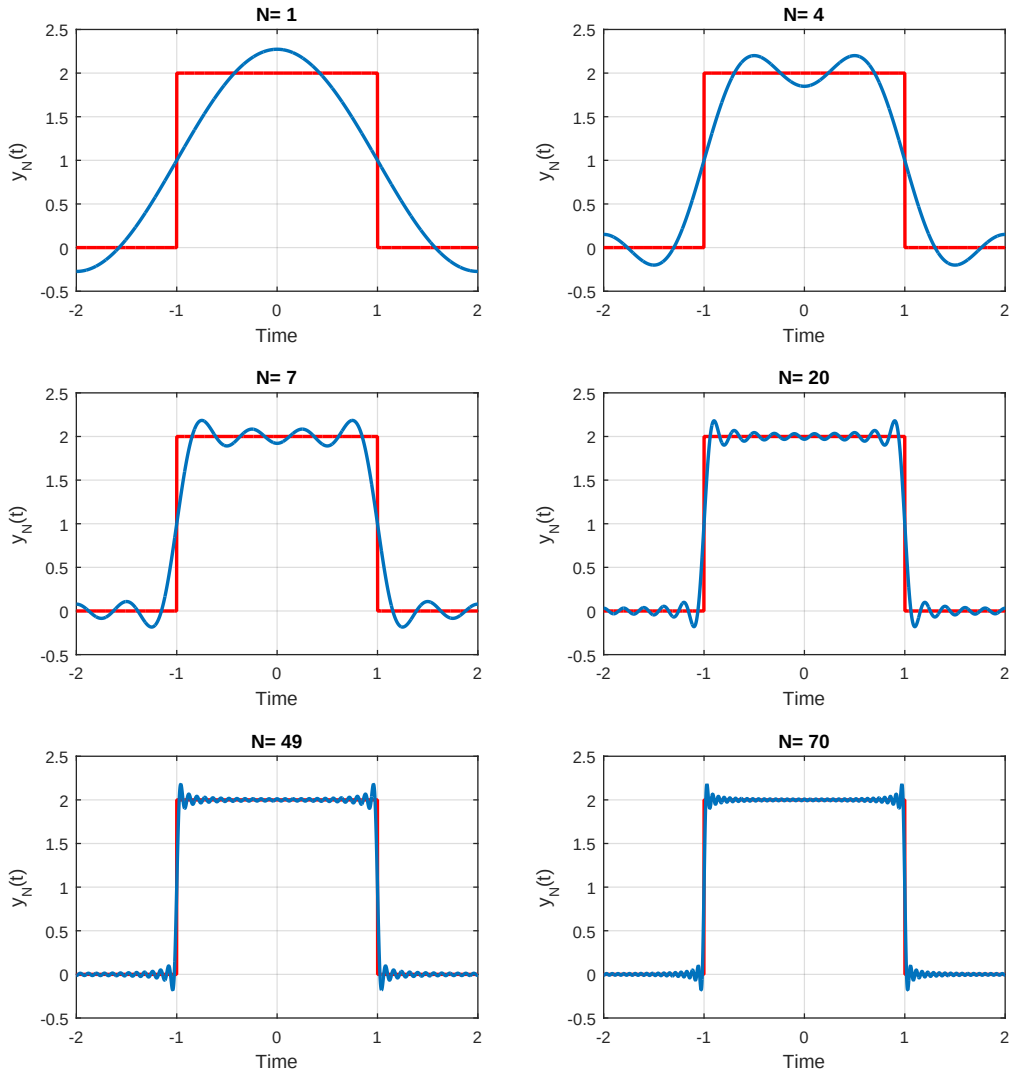

Figure 3.3. Gibbs Phenomenon: A demonstration for square wave.

where the Fourier coefficients $\hat{f}(n)$, a_n, b_n are given by their usual definition as

$$\begin{cases} \hat{f}(n) & := \frac{1}{L}\int_0^L f(x)e^{-2\pi inx/L}dx \\ a_n & := \frac{2}{L}\int_0^L f(x)\cos\left(\frac{2\pi nx}{L}\right)dx \\ b_n & := \frac{2}{L}\int_0^L f(x)\sin\left(\frac{2\pi nx}{L}\right)dx \end{cases} \tag{3.19}$$

Using basic calculus we can now evaluate the summation around the break-point, and take the limits to get

$$\lim_{N\to\infty} S_N f\left(x_0 + \frac{L}{2N}\right) = f(x_0^+) + a.(0.0894) \tag{3.20}$$

and

$$\lim_{N\to\infty} S_N f\left(x_0 - \frac{L}{2N}\right) = f(x_0^-) + a.(0.0894) \tag{3.21}$$

As can be noticed in Figure 3.3, as the number of terms increases, the width of the overshoot decreases, but the height converges to a fixed amount. This fixed amount, as calculated in Equations (3.20) and (3.21), shows that the overshoot and the undershoot on either side of the discontinuity equal to $a.(0.0894)$. Primarily, Gibbs phenomenon reflects the inherent difficulty in approximating to a discontinuity using a finite number of continuous sinusoidal basis functions. The smoothness of a function is closely related to the rate of decay of Fourier coefficients at higher frequencies. Functions with discontinuity will have slow convergence of the Fourier series due to slowly decaying coefficients. Converging coefficients or coefficients with absolute convergence will have uniformly convergent approximations by Weierstraas M-test and would subsequently not show any oscillatory behavior. In signal processing, the Gibbs phenomenon is frequently encountered in filter design where Brick wall characteristics are generally required of most filters, which have sharp transition from passband to stopband. An ideal lowpass filter translates to a sinc function $(sin(x)/x)$ in the time domain, with an infinite duration. In practical designs, this sinc function is truncated appropriately to realizable time durations, which then leads to wiggles at

the transition in the frequency domain. This problem is ameliorated usually by using smoothly tapered windowing techniques like Hanning, Blackman, Kieser windows, etc. Other methods attempt to get a smoother summation of the Fourier series, such as Fejr summation or Riesz summation, [32] or by applying a wavelet transform using Haar basis functions, [33].

3.3 Numerical Optimization Solution

The blips in the least square fit to the bang-bang profile, at the break-point, are detrimental to performance in the design of shaped profiles. These blips symbolize the non-uniform decay of the coefficients of the basis function harmonics. Thereby, the overshoots and undershoots at the transition occur from the energy in the signal constituted by higher frequency harmonics. So, when a penalty is added in the cost function to remove energy at natural modes of the system, more energy gets pumped into these higher energy peaks. This results in nervous looking shaped profiles at the transition from acceleration to deceleration phase and eventually demand high intermittent torques to drive the system to the desired end point.

As shown in section 3.1.1, the trajectory design routine solves a multiobjective optimization problem where it determines the coefficients for the chosen basis function that minimize the appropriately defined penalty function. This implies that the coefficients can not be directly manipulated through the use of windowing techniques or smoother summation methods and the solutions described in section 3.2.2 don't lend themselves particularly useful to the command shaping formulation. Therefore,

in this work a method is presented to resolve the Gibbs phenomenon through optimization to obtain smoother bang-bang profile approximations. This is achieved by constraining the penalty function and laying out a numerical optimization framework that solves for basis function coefficients iteratively while subjected to linear and nonlinear constraints.

Objective Function and Constraints

The analytical formulation as proposed in [13], [14] involves scaling of the coefficients, obtained from optimization, to normalize the peaks of the shaped profile and satisfy Equation (3.4). However, the coefficients can be prescaled to normalize the function being approximated and include it in the cost function. Doing this would force the choice of coefficients such that there are no peaks crossing the bound. We begin with an initial set of coefficients,

$$B_l = [B_1, B_2, ...B_L] \tag{3.22}$$

and as earlier, we find scale factor SF from Equation (3.24) to get

$$B_l^* = [B_1^*, B_2^*, ...B_L^*] \tag{3.23}$$

where

$$B_i^* = B_i/SF, \tag{3.24}$$

L is the total number of harmonic coefficients. Now we can write the updated cost function as,

$$J = \frac{1}{T_f}\left[\int_0^{T_f}[u_{bb} - f^*(t)]^2 dt\right] + \rho\sum_{i=1}^{11M}(\omega_i T_f)^2|F^*(\omega_i T_f)|^2, \tag{3.25}$$

where

$$f^*(t) = \sum_{l=1}^{L} B_l^* \Phi_l^*(t) \tag{3.26}$$

and u_{bb} denotes a complete cycle of the bang-bang profile. For now, we just focus on the least square fit to a bang-bang function to look at the difference due to prescaling of the synthesized function f, thus, ρ in Equation (3.25) is zero. Figures 3.4 and 3.5 show the approximated profiles with Ramped Sinusoid basis functions. These profiles represent the acceleration input required to displace the target system by a unit magnitude. As mentioned in subsection 3.1.2 and in Equation (3.15), the acceleration profiles need to be scaled to overcome the loss of energy due to errors in approximation, and hence the obtained profiles have peaks greater than unity.

Looking at the two profiles, it can be noticed that bounding the force function amplitudes gets rid of overshoots, however, ringing in the form of undershoots still persists. Also, in Figure 3.5, it can be seen that the decay of coefficients is faster than the case in Figure 3.4 but there is still non-uniformity at higher frequencies. So, constraining the function alone doesn't serve the purpose of smoother fits.

The Least Square Error (LSE) formulation is an $\mathbf{L_2}$-norm and is basically minimizing the sum of squared error of the fit. Statistically speaking, LSE is more stable, i.e., it is not affected by any outliers or a small change in one of the datums. However,

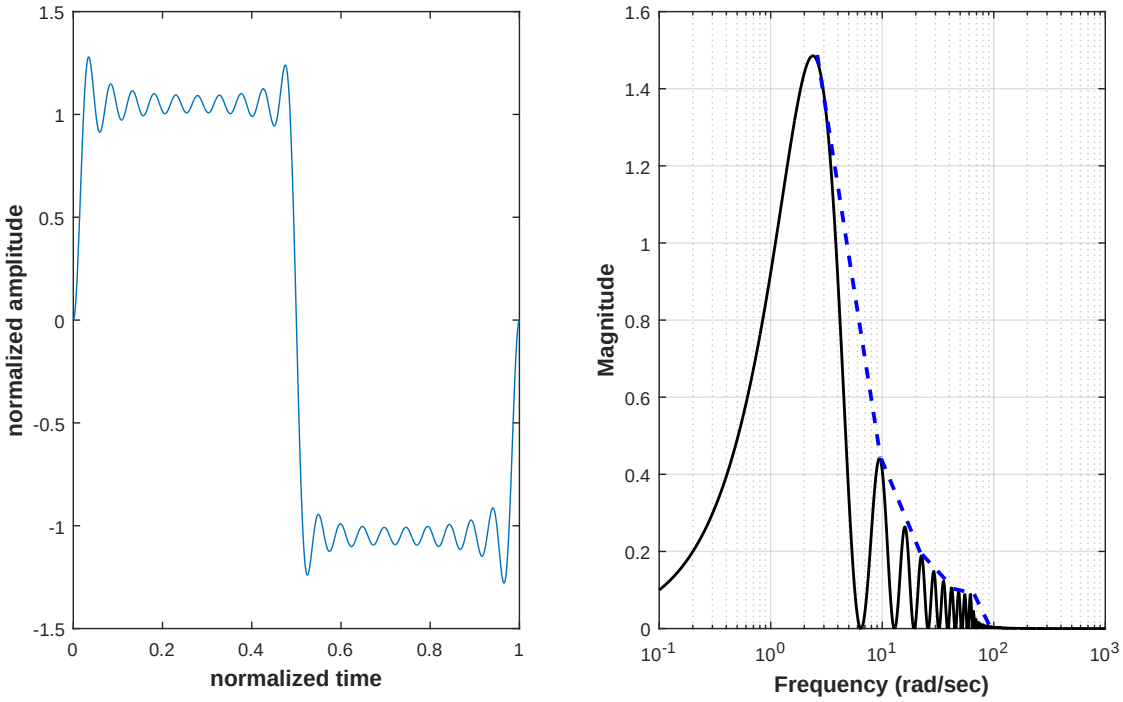

Figure 3.4. Bang-bang approximation using analytical formulation.

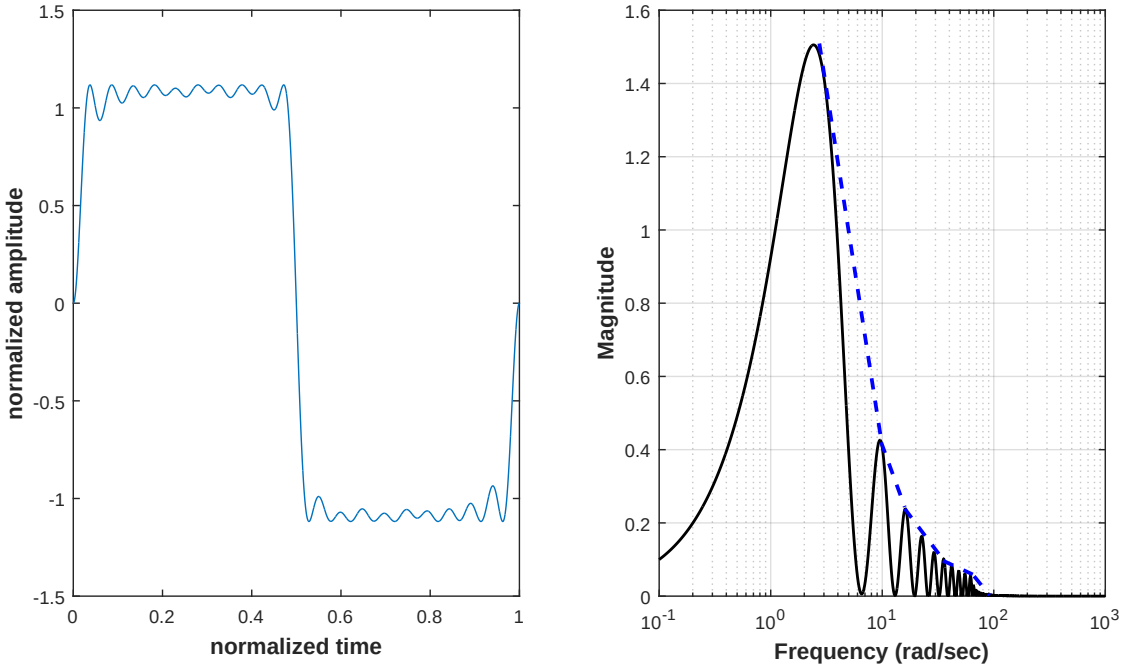

Figure 3.5. Bang-bang approximation using constrained formulation.

LSE is not robust. By virtue of looking at square of error, it puts more emphasis on residuals that are larger. This increases the rate of transition at the discontinuity, $(f(0^+) + f(0^-))/2$, and provides acute or high derivatives at the cost of not approximating the function well at points of overshoots or undershoots. A truncated Fourier series, as analyzed in section 3.2.2 is also the best approximation to the desired function in an $\mathbf{L_2}$ sense. Because there is a limit to how large a value the derivative of a trigonometric polynomial can assume, it bodes well to fit a polynomial by gathering speed at transition across a discontinuity and overshooting on either side.

In this study, however, smoothness of approximation is more important in the sense of command shaping for reasons outlined earlier. Therefore, we shift our focus to $\mathbf{L_1}$-norm function, also termed as Least Absolute Deviation (LAD). It basically aims to minimize the sum of absolute errors in the fit, thereby weighting all the errors equally. Unlike $\mathbf{L_2}$-norm, $\mathbf{L_1}$-norm can not be solved analytically and needs more computational resources to find a solution. However, since the shaped functions are generated offline, it does not pose an issue. A numerical optimization approach is taken to obtain the $\mathbf{L_1}$ function solution. Under this, the first objective of the cost function can be rewritten as,

$$J_{L1}^{bb} = \frac{1}{T_f} \sum_{i=1}^{N} |u_{BB}(t_i) - f^*(t_i)| \tag{3.27}$$

where $f^*(t)$ is the same as defined for Equation (3.25) and $N = T_p/dt$, dt is the discrete step size for evaluation of numerical error points. In Figure 3.6, we can notice that the ringing effects in the approximation have disappeared and also that the rate of decay at higher frequency is now uniform. This has resulted in uniform convergence

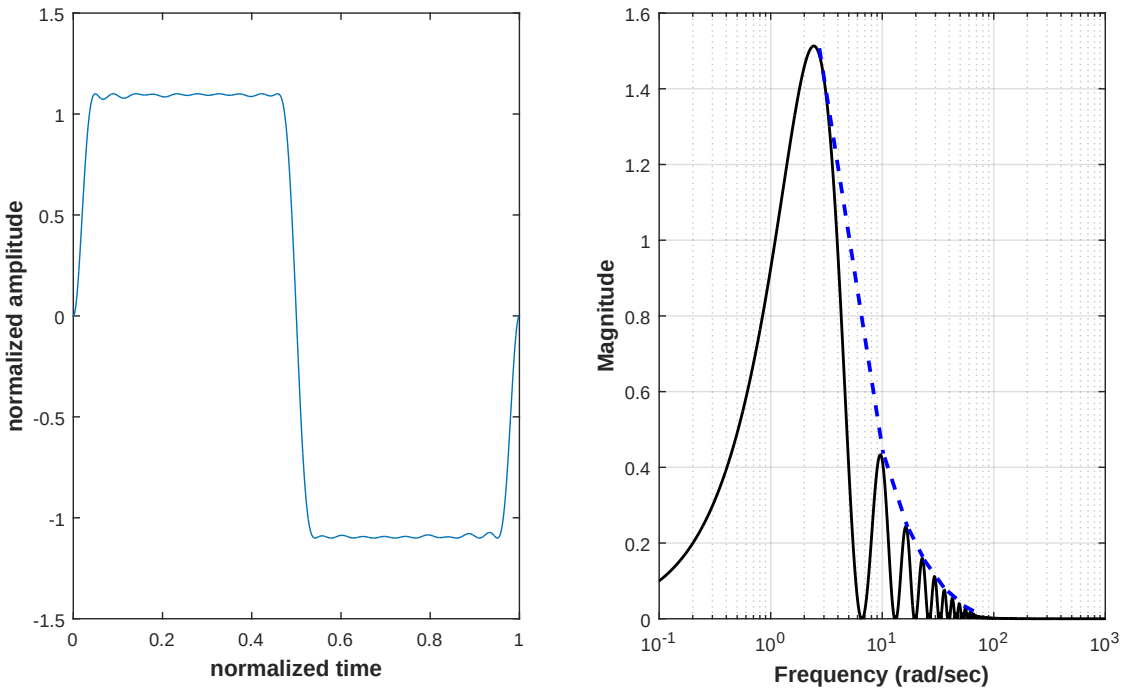

Figure 3.6. Bang-bang approximation using numerical L1-norm formulation.

of the fit across each peak of the synthesized profile. Similar results are obtained for shaping the bang-bang profile using Versine basis functions, Figure 3.7. Therefore, we have resolved the ringing artifact issue through applying a constrained numerical optimization approach. The overall cost function including the second objective can be given as,

$$J_{L_1} = J_{L1}^{bb} + \underbrace{\frac{\rho}{T_P}\sum_{i=1}^{kM}(\omega_i T_f)^2|F^*(\omega_i T_f)|^2}_{J^{\omega_n}} \tag{3.28}$$

where J^{ω_n} is the objective function for penalizing the frequency content around the natural frequency ω_n, k is the number of equally distributed points around each of the M natural frequencies of the system.

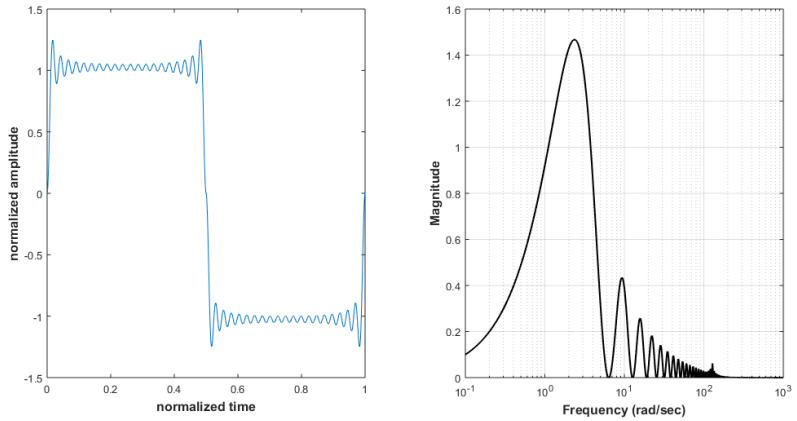

(a) Bang-bang approximation using analytical formulation

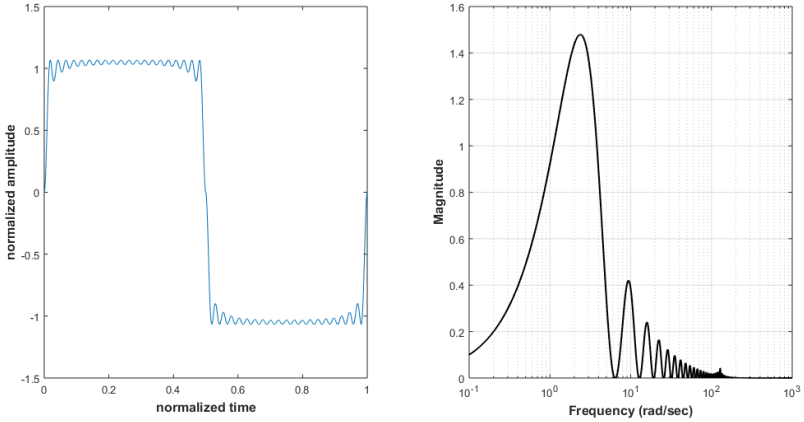

(b) Bang-bang approximation using constrained formulation.

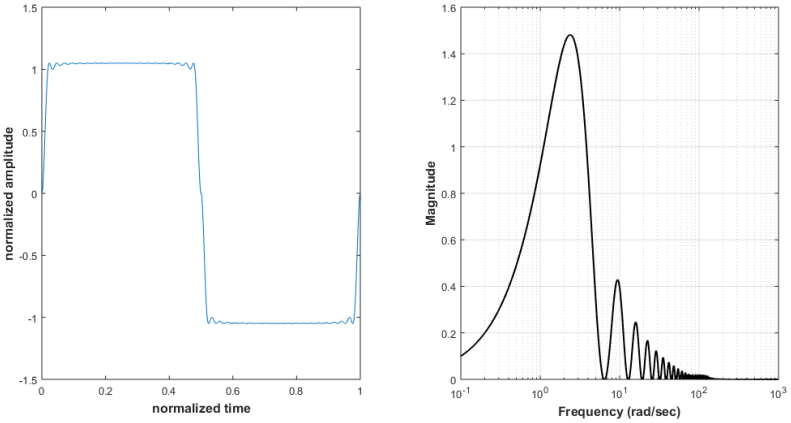

(c) Bang-bang approximation using numerical L1-norm formulation.

Figure 3.7. Least Absolute Error fit using Versine basis function.

The general layout of the proposed method can now be summarized as in Figure 3.8,

$$\min_{B_l} \; J_{L_1}(B_l, T_f, \omega_n, \rho) \text{ such that } \begin{cases} -1 \leq \sum_{l=1}^{L} B_l^* \Phi_l^*(t) \leq 1 \end{cases} \tag{3.29}$$

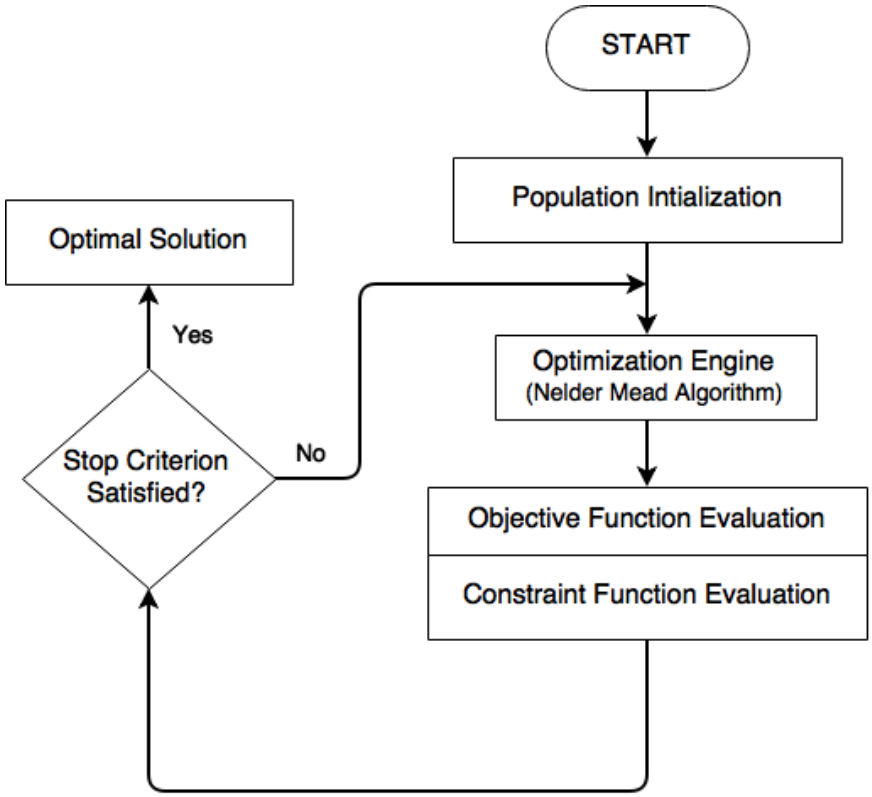

Figure 3.8. Numerical Optimal Solution Routine.

In order to determine the attenuation of frequency content around each of the flexible modes, the expressions for J^{ω_n} in the cost function J_{L_1} can be calculated using a simple Fourier transform as,

$$F(\omega) = \int_0^{T_f} F^*(t) e^{-i\omega t} dt \tag{3.30}$$

where $F^*(t)$ is denoted the same as in Equation (3.26) and T_f again represents the move time. For Versine, $T_f = T_V n_{seg}$, where n_{seg} is the number of segments in the

profile and T_V is the move time of each of these individually shaped segments. Now, the respective frequency spectra expressions for the Ramped Sinusoid and Versine can be given by

$$|F^*(\omega)|_{RS} = \left| \frac{2\sin(\omega T_f/2) - \omega T_f \cos(\omega T_f/2)}{(\omega T_f/2)^2} \sum_{l=1}^{L} \frac{B_l^* \alpha_l}{\alpha_l^2 - (\omega T_f)^2} \right| \tag{3.31}$$

and

$$|F^*(\omega)|_{V} = \left| \frac{2(2\pi)^2 \sin^2(\omega T_V/2)}{(\omega T_V)} \sum_{l=1}^{L} \frac{B_l^* l^2}{(2\pi l)^2 - (\omega T_V)^2} \right| \tag{3.32}$$

3.4 Influence of Weighting Factor

Having established a solution for Gibbs phenomenon, it is important to understand the tradeoffs that occur in the process. Especially, a closer look is required to inspect the behavior of the second objective in the optimization, i.e., removal of frequency content around the resonant modes. The weighting factor, ρ, between the two competing objective functions governs the overall nature of the shaped input. More penalty on frequency attenuation will remove more and more energy at the spectral location of the natural modes, thereby giving us better residual vibration performance profiles but commands that are more skewed in comparison to the reference bang-bang. Because of removal of more energy, higher penalty would mean higher scaling of the normalized input to reach the desired destination point. This would in turn impose higher demand on the actuators to meet the peak acceleration input without introducing additional nonlinearities due to saturation.

For the cost function in Equation (3.28), it would be intuitive to think that higher weighting factor would essentially lead to more attenuation and better performance. However, in a multiobjective setting and due to the nature of tradeoffs, that might not necessarily be the case. Increasing ρ beyond a certain value could skew the acceleration profile such that no more attenuation could be exercised without increasing the error of fit. In such a case, increasing the penalty would adversely affect the attenuation and the optimization would search in a solution space where it attempts to minimize the fitness error first. There is a need to better understand this tradeoff against ρ. Therefore, in this section, we have attempted to quantify the variation of attenuated energy at a frequency window and the peak input acceleration with ρ. This study will generate mappings that could be used to select optimum weighting factor based on performance requirements and actuator limits. These mappings have also been utilized to compare the performance of the constrained numerical approach in reference to the analytical solution.

Since the flexible-joint robot in this study has two resonant modes, we attempt to attenuate energy at both the modes in the design of shaped profiles. A good estimate to calculate the effective attenuation through a single parameter is to obtain the scaled magnitude as,

$$|F(\omega_{12})| = \omega_1 |F(\omega_1)| + \omega_2 |F(\omega_2)| \tag{3.33}$$

where $F(\omega_1)$ and $F(\omega_2)$ are the average magnitude at the two attenuated spectral window around each natural frequency and are calculated by,

$$|F(\omega_n)| = \sum_{i=1}^{N} |F(\omega_i)| \Big/ N \tag{3.34}$$

where ω_i is calculated at N equally divided points between $0.9\omega_n \leq \omega_i \leq 1.1\omega_n$.

Figures 3.9 and 3.10 illustrate the effect of ρ on Γ as defined for each of the two basis functions in Equations (3.15) and (3.16), and the scaled attenuation. Γ here is indicative of the peak acceleration in the shaped input scaled on a unit bang-bang acceleration profile. It can be observed that these variations against ρ are largely monotonic for each of the four cases with larger attenuation leading to larger desired acceleration peaks. However, our interest lies in exploring the effect of the constrained numerical optimization approach on these parameters in comparison to the conventional analytical method to generate shaped inputs. From the data markers in Figure 3.9(a) and Figure 3.9(b), it can be noted that for a similar Γ value of 30, the average attenuation achieved in case of the numerical approach, 8.89 dB, is larger than its counterpart in the analytical method, 9.178 dB. Also, a given attenuation of the order of 8.2 db, is designed at a lower Γ value of 46.66 in the constrained numerical optimal solution compared to 70.74 in the closed form solution. Similar observations can be made for the Ramped Sinusoid profiles in Figure 3.10. Between Figures 3.9 and 3.10, it can also be noted that the Ramped Sinusoid profiles generally are able to achieve better attenuation at the desired frequencies than their Versine counterparts. Although more exploration is needed to reason this behavior, initially it is suspected that the symmetrical nature of Versine profiles does not allow as good a tradeoff

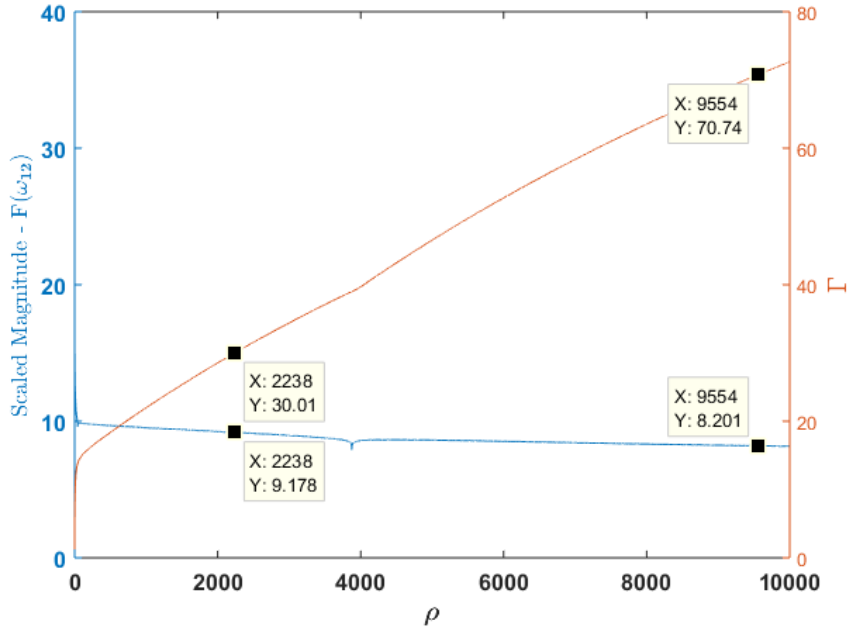

(a) Closed form analytical formulation.

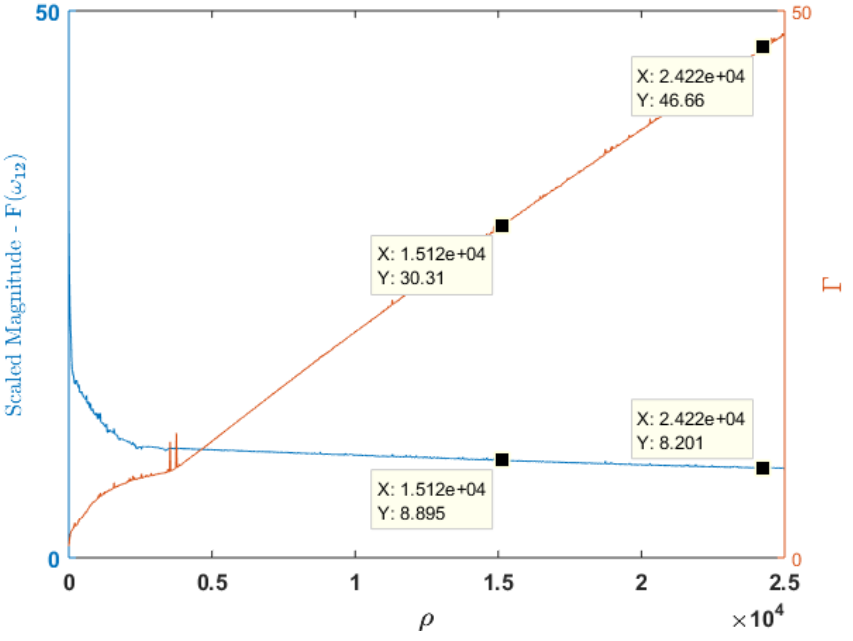

(b) Constrained numerical optimization formulation.

Figure 3.9. Influence of ρ on shaped profiles: Versine.

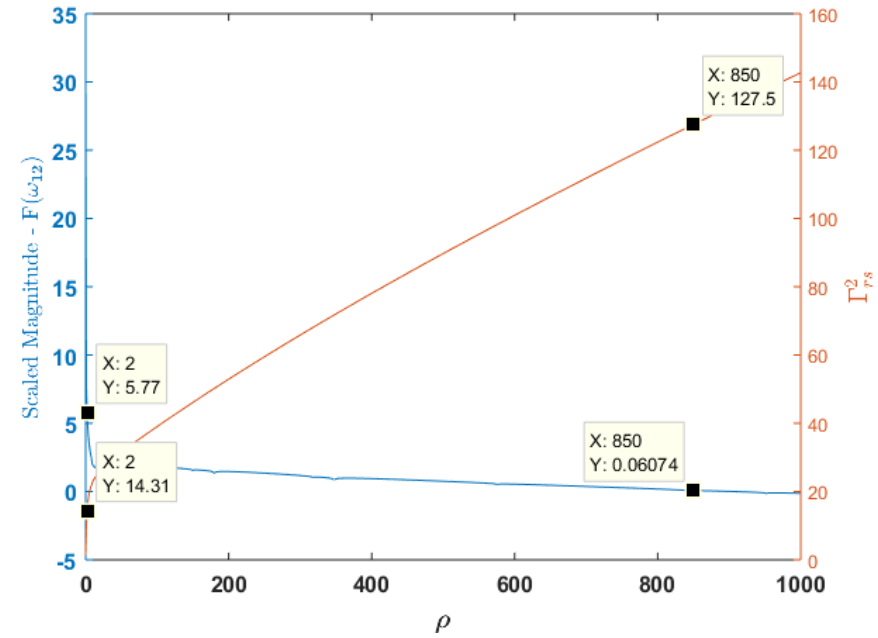

(a) Closed form analytical formulation

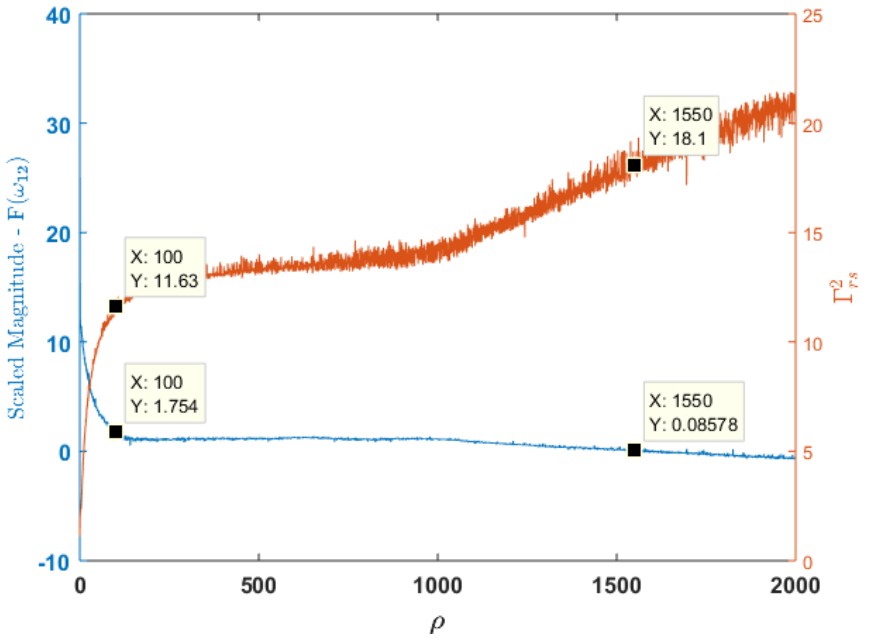

(b) Constrained numerical optimization formulation.

Figure 3.10. Influence of ρ on shaped profiles: Ramped Sinusoid.

between minimizing the error of fit to the bang-bang and removing energy at spectral location of flexible modes. In the next chapter, the implications of this difference between the two characteristic basis functions on reducing the residual vibrations in the robot would also be investigated through experimental analysis.

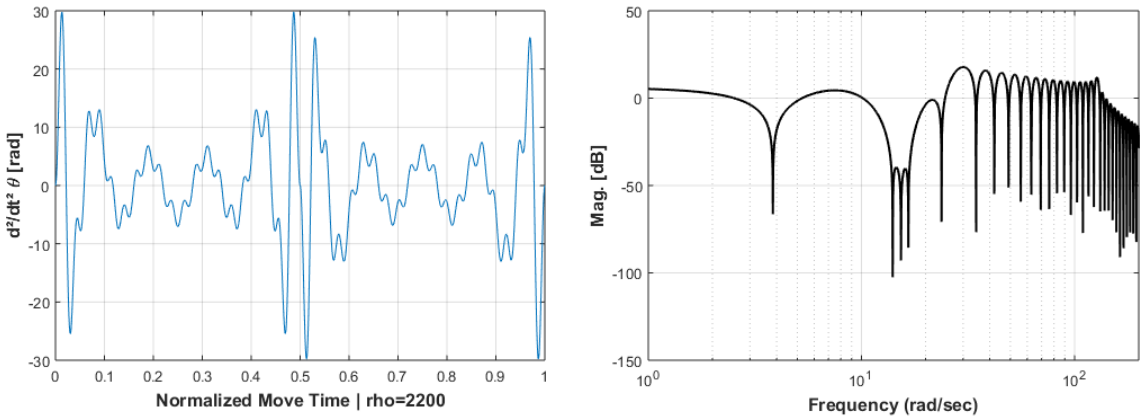

(a) Closed form analytical formulation

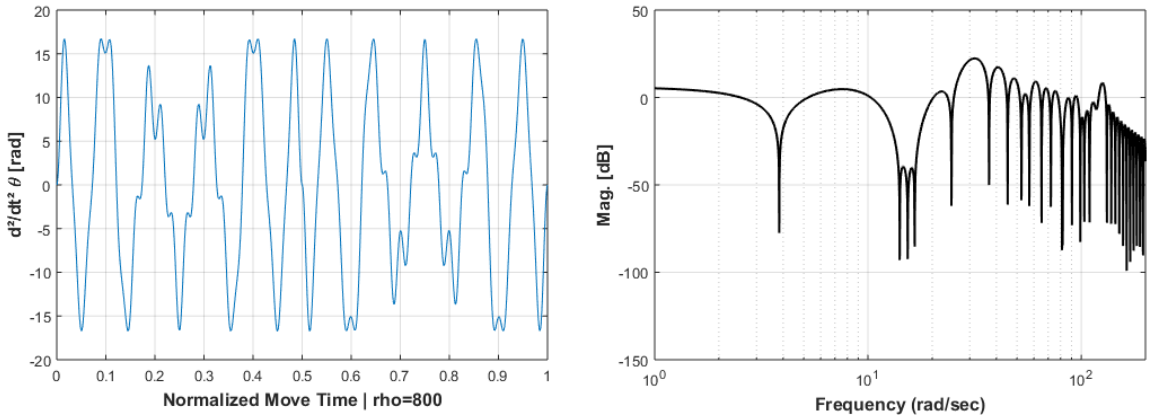

(b) Constrained numerical optimization formulation.

Figure 3.11. Relative redistribution of energy at intermediate modes: Versine.

It would seem counter intuitive at first that there is not a penalty of some sort to smoother approximation of the bang-bang function. Comparatively more energy

removal should imply the need for higher scaling and in turn higher input peaks or that with a lower demand on input peak the attenuation should be compromised. To better understand this peculiar tradeoff, a closer look is taken for a sample case. In Figure 3.11, for a unit displacement of the end effector, the inputs are designed to have similar energy at a window around the two natural frequency modes, viz. 3.79 rad/s and 15.3 rad/s. A maximum acceleration in the analytical input is at 30 rad/s^2 and in the constrained numerical approach case it is 16.5 rad/s^2. We can, however, notice the pattern observed earlier in Figure 3.6, where the energy at higher frequency components is uniformly decreasing. This pattern stays put even after penalizing for critical frequency content removal and in effect redistributes the energy to intermediate frequencies, between 20 and 50 rad/s in Figure 3.11(b). Doing this permits the removal of intermittent surges or spikes in the input at the discontinuity. In that sense, we are able to design inputs that need not exploit the maximum available acceleration and also do the intended job of suppressing residual vibrations by neglecting the joint resonant frequencies.

4. APPLICATION TO THE ROBOT

Now that the proposed numerical approach for command shaping has been studied in respect to major attributes of the input, attenuated energy and maximum desired force, this chapter will focus on validating the performance of the proposed approach and establishing comparative analysis to the conventional command shaping solution. Section 4.1 first outlines the setup of the robot experimental platform, then in Section 4.2 multiple performance metrics have been defined and discussed to quantify performance of the test profiles. Section 4.3 discusses a simulation model of the robot system and also describes the effect of parametric mismatch between the controller and the plant. Lastly, in Section 4.4, the vibration performance of shaped commands has been tested and analyzed in experiments on the two-link robot.

4.1 Robot Experimental Set-up

Each of the two joints of the experimental robot, setup in the Ruth and Joel Spira Laboratory for Electromechanial Systems at Purdue University, is actuated by a permanent magnet DC motor. The first link is driven by a motor with maximum torque of 2.47 Nm at 21.2 A and a torque constant of 0.118 Nm/A. The second link is driven by a frameless Inland T-3108-A torque motor that has a torque constant of 0.61 Nm/A and a maximum torque of 1.35 Nm at about 2 A. Each motor is driven

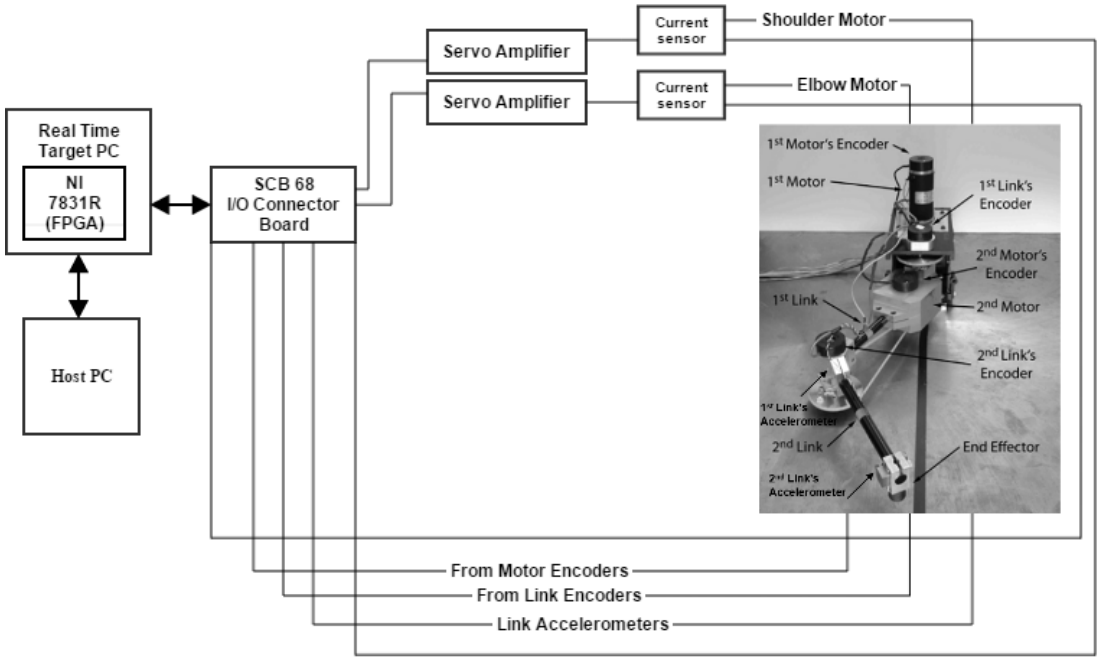

Figure 4.1. Schematic of the two-link robot experiment set-up.

by an Advanced Motion Control brushless pulse-width-modulated transconductance servo amplifier that converts input voltage commands into current commands. To measure the positions of the two joints and two links, four incremental optical encoders each having a resolution of 4000 counts per revolution have been used. Finite differences with a fourth-order Butterworth filter are used to obtain velocities. Two capacitive accelerometers, with a sensitivity of $\pm 2g$, have been mounted at the end of each link length to measure accelerations. These measurements have been used in defining and calculating the performance metrics that are used to characterize vibration performance. Two current sensors have also been utilized to measure motor current, which is proportional to motor torque.

National Instruments' LabVIEW software running in conjunction with the Real Time Module is used for data acquisition. A schematic of the overall setup is shown in Figure 4.1. The user interacts with a host PC, where the controller is programmed. The target PC executes the controller to ensure fast real-time processing, and is connected with NI 7831R module, which provides multiple digital and analog I/O to collect sensor data and send out current commands to the motors. These input/output channels are controller by a reconfigurable Field-Programmable Gate Array (FPGA), which enables fast preprocessing and sampling of the input signals. The controller on the LabVIEW real-time system has been configured to sample at 2 kHz.

For simulation analysis and experimental verification, a point-to-point movement of both links from the initial state $\theta_{1,i} = 0$ rad and $\theta_{2,i} = 0$ rad to the final state of $\theta_{1,f} = 1.2$ rad and $\theta_{2,f} = 1.2$ rad with a move time of 2 seconds is chosen as the benchmark problem.

4.2 Performance Metrics

To study the effectiveness of the generated commands, it is necessary to be able to measure the residual vibration in the system. The two most important characteristics of residual vibration are (1) the vibration amplitude and (2) the settling time. Residual vibration measurement for nonlinear, multimode systems can be tricky and so far most of the vibration measurement methods presented in the literature discuss linear single-mode systems. For such systems, closed-form expressions for settling time or residual vibration can be analytically derived. Moreover, most of these methods are

applicable to input shaping techniques [11], which derive information from the system model to generate the shaped input. Vibration amplitudes and settling times for single-mode system are usually calculated by fitting dissipation envelope to the response. However, for a multimode, nonlinear system, where the envelope depends on coupling and interaction of the modes, application of such methods is not straightforward. Therefore, in this work, an attempt has been made to calculate residual vibration through single standard parameters, in reference to a two-link flexible-joint robot, through experiments. In effect, this is achieved by considering the motion of end-effector point B in Figure 4.2. We need to do a basic vector analysis to derive the planar acceleration of the end-effector in terms of available sensor measurements. Note that the base of link 2, point A, is a non-inertial frame of reference. Therefore, we can represent the system using the following vector notation. For position vector

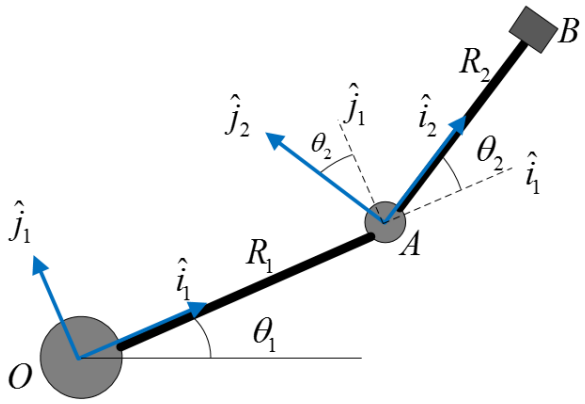

Figure 4.2. Vector diagram of the robot kinematic chain.

$\overrightarrow{OA} = R_1\hat{i}_1$ and the velocity vector $\dot{\overrightarrow{OA}} = R_1\omega_1\hat{j}_1$, the acceleration vector can be written as,

$$\begin{aligned}\ddot{\overrightarrow{OA}} =& R_1\omega_1^2\hat{k}_1 \times \hat{j}_1 + R_1\dot{\omega}_1\hat{j}_1 \\ =& - R_1\omega_1^2\hat{i}_1 + R_1\dot{\omega}_1\hat{j}_1\end{aligned} \tag{4.1}$$

Similarly, for the end-point B, the acceleration vector can be derived by:

$$\begin{aligned}\overrightarrow{OB} =& \overrightarrow{OA} + \overrightarrow{AB} \\ =& R_1\hat{i}_1 + R_2\hat{i}_2\end{aligned} \tag{4.2}$$

$$\begin{aligned}\dot{\overrightarrow{OB}} =& R_1\frac{d\hat{i}_1}{dt} + R_2\frac{d\hat{i}_2}{dt} + \dot{R}_1\hat{i}_1 + \dot{R}_2\hat{i}_2 \\ =& R_1\omega_1\,\hat{k}_1 \times \hat{i}_1 + R_2\omega_2\,\hat{k}_2 \times \hat{i}_2\end{aligned} \tag{4.3}$$

$$\begin{aligned}\ddot{\overrightarrow{OB}} =& R_1\omega_1^2\hat{k}_1 \times \hat{j}_1 + R_2\omega_2^2\hat{k}_2 \times \hat{j}_2 + R_1\dot{\omega}_1\hat{j}_1 + R_2\dot{\omega}_2\hat{j}_2 \\ =& - R_1\omega_1^2\hat{i}_1 - R_2\omega_2^2\hat{i}_2 + R_1\dot{\omega}_1\hat{j}_1 + R_2\dot{\omega}_2\hat{j}_2\end{aligned} \tag{4.4}$$

$\ddot{\overrightarrow{OB}}$ can be represented in base frame of link 2 as,

$$\ddot{\overrightarrow{OB}} = (*)\,\hat{i}_2 + (*)\,\hat{j}_2 \tag{4.5}$$

where * is a short-hand notation for components that need to be calculated. So, the translation between the two frames can be given by,

$$\begin{aligned}\hat{i}_2 &= \cos\theta_2\,\hat{i}_1 + \sin\theta_2\,\hat{j}_1 \\ \hat{j}_2 &= \sin\theta_2\,\hat{i}_1 + \cos\theta_2\,\hat{j}_1\end{aligned} \tag{4.6}$$

and the transpose matrix from $\begin{bmatrix} \hat{i}_1 & \hat{j}_1 \end{bmatrix}$ to $\begin{bmatrix} \hat{i}_2 & \hat{j}_2 \end{bmatrix}$ as,

$$\begin{bmatrix} \hat{i}_1 \\ \\ \hat{j}_1 \end{bmatrix} = \underbrace{\begin{bmatrix} \cos\theta_2 & \sin\theta_2 \\ \\ -\sin\theta_2 & \cos\theta_2 \end{bmatrix}}_{T} \begin{bmatrix} \hat{i}_2 \\ \\ \hat{j}_2 \end{bmatrix} \tag{4.7}$$

Now, we have

$$\begin{aligned} \ddot{\overrightarrow{OB}} &= \begin{bmatrix} -R_1\omega_1^2 & R_1\dot{\omega}_1 \end{bmatrix} \begin{bmatrix} \hat{i}_1 \\ \\ \hat{j}_1 \end{bmatrix} + \begin{bmatrix} -R_2\omega_2^2 & R_2\dot{\omega}_2 \end{bmatrix} \begin{bmatrix} \hat{i}_2 \\ \\ \hat{j}_2 \end{bmatrix} \\ &= \left(\begin{bmatrix} -R_1\omega_1^2 & R_1\dot{\omega}_1 \end{bmatrix} T + \begin{bmatrix} -R_2\omega_2^2 & R_2\dot{\omega}_2 \end{bmatrix} \right) \begin{bmatrix} \hat{i}_2 \\ \\ \hat{j}_2 \end{bmatrix} \\ &= \begin{bmatrix} -R_1\omega_1^2\cos\theta_2 + R_1\dot{\omega}_1\sin\theta_2 - R_2\omega_2^2 & -R_1\omega_1^2\sin\theta_2 + R_1\dot{\omega}_1\cos\theta_2 + R_2\dot{\omega}_2 \end{bmatrix} \begin{bmatrix} \hat{i}_2 \\ \\ \hat{j}_2 \end{bmatrix} \end{aligned} \tag{4.8}$$

Equation (4.8), thus, allows us to obtain the net translatory acceleration at the end-tip in terms of available measurements of angular positions and angular velocities from the encoders and linear acceleration components from the accelerometers. The vibration amplitude can now be determined using one of the following two methods. First, in the acceleration domain, the residual amplitude can be obtained by:

$$a_{rv}(t) = max(a(t)) - min(a(t)) \tag{4.9}$$

where

$$a = \sqrt{a_x^2 + a_y^2} \tag{4.10}$$

with a_x and a_y representing the $\hat{i}_2$ and $\hat{j}_2$ components of $\ddot{\overrightarrow{OB}}$ and $t_i \leq t \leq t_f$, with t_i denoting the command completion time and t_f the overall run time of the experiment. The net excursion can also be written in terms of maximum residual displacement of a response from the equilibrium as

$$\Delta_{xy} = \sqrt{\Delta_x^2 + \Delta_y^2} \tag{4.11}$$

where Δ_x, Δ_y are the deflections about the equilibrium after the completion of the command.

Lastly, to study the dissipation performance of the vibration in a response, a settling time measure is defined. It is calculated by scanning the acceleration response in Equation (4.10) to find the maximum time, t_s, for which the response stays above the vibration tolerance. This tolerance is designed by experience and looking at the noise floor in measurements of the constituting components in the signal. These three methods have been used to characterize and compare the performance of several different shaped profiles.

4.3 Simulation Analysis

A simulation model of the two-link robot is utilized to evaluate the system response under different parametric variations. In the simulation environment, practical limitation that are encountered in the real system have also been incorporated to maintain best possible consistency between the simulated and the experimental results. Identical to the specifications in Section 4.1, a sampling rate of 2 kHz is used for the

simulated controller and the quantization effect of four encoders with finite resolution (4000 steps/revolution) is considered in simulated sensor feedback. In addition, the quantization due to Digital-to-Analog conversion of current command signals through the NI 7831R is also included in the model. Since encoder measurements only provide position feedback, the online velocity calculation through backward finite differences in LabVIEW system is emulated similarly in the simulation environment. A 4^{th}-order Butterworth filter with a cut-off frequency at 60 Hz is included to reduce of the noise due to numerical differentiation. Thus, small phase delays due to the filter and finite differences are introduced in the system.

To meaningfully assess the extent to which the vibration suppression performance of the shaped input can be predicted by the spectral magnitude of the critical frequencies, it is important to look at system response against varying attenuation levels. In Figure 4.3, for the closed-form ramped sinusoid profiles, the residual oscillations in the simulated response has been mapped against increasing weighting factor ρ. It is important to note here that only peak-to-peak residual accelerations have been considered to quantify the vibration amplitude. For simulation study, residual acceleration has been used to represent the amplitude of vibration.

Since the computed torque method includes a model-based portion, the controller has Coulomb friction terms and, thereby, a sign$(\cdot)$ function appears in the control law. This function can result in chattering in the control output and although this effect is ameliorated by amplifier and motor dynamics in the real experiment, the chatter directly influences the motor torques in simulations. In Figure 4.3(a), the simulation

results show the variation in settling time and residual acceleration, as defined in Section 4.2, with ρ when the Coulomb friction terms in the model-based portion have been neglected. To understand the effect of parameter variations, in Figure 4.3(b), the results are recorded for a case with purposely designed parameter mismatch between the model-based part of computed torque and the robot plant. Since most of the inaccuracy lies in estimating friction effects, the mismatch has been specifically built in friction and damping parameters in the model-based part, where the viscous damping matrix elements are increased by 50% and to still keep the Coulomb friction low, 20% of estimated values for the Coulomb friction are used. The parameters in the plant, however, were not changed. Therefore, in the first case, Figure 4.3(a), apart from the neglected Coulomb friction and small differences between the complete and the reduced Lagrangian model which is used to derive the trajectories, the dynamic behavior is fully known. This, however, is not possible in experiments where the actual physical parameters are not known and the mathematical model only imperfectly captures the robot behavior.

Two important observations can be made from Figure 4.3: the vibration performance largely improves with increasing ρ, in both respects t_s and a_{rv}, until a point where saturation of actuators comes into effect, and the performance deteriorates quickly. For the first case, Figure 4.3(a), in the absence of friction effects in the controller, the settling times and residual amplitude are both smaller than their counterparts in Figure 4.3(b). Also, in the case of mismatched parameters, the saturation effects come into play at a relatively smaller value of ρ. Through more advanced

design of experiments or nonlinear identification methods such as a neural network, a specific set of mismatched parameters can be built in the simulation model so that it could more closely predict the experimental response of the robot.

4.4 Experimental Results

To gain better insight on performance of the proposed numerical approach and how it compares to the closed-form method of command shaping, it was decided to test and study various shaped profiles in application to the robot platform. After looking at design simulations to compare and highlight important features of the two shaping methods, the analysis in this is focused towards evaluating the performance of the two shaping routines. Since the simulation model does not lend a lot of insight due to susceptibility to parameter mismatch between the feedforward block and the plant, to draw more meaningful and consistent inferences, only experimental results are discussed in this section.

Multiple sets of command profiles, both for the versine and the ramped sinusoid, have been compared under two fundamental conditions. Tables 4.1 and 4.2 list the basis of comparison on the left and the respective performance of each profile in terms of the three metrics, defined in Section 4.2, on the right. In the first condition, our interest is in constraining the maximum commanded acceleration $\ddot{\theta}_{d,max}$ or Γ in the input and then evaluating the amount of vibration in the system. In contrast, in the second condition, the focus is on investigating cases with similar levels of spectral magnitude or scaled attenuation at the system natural frequency, as defined in Equa-

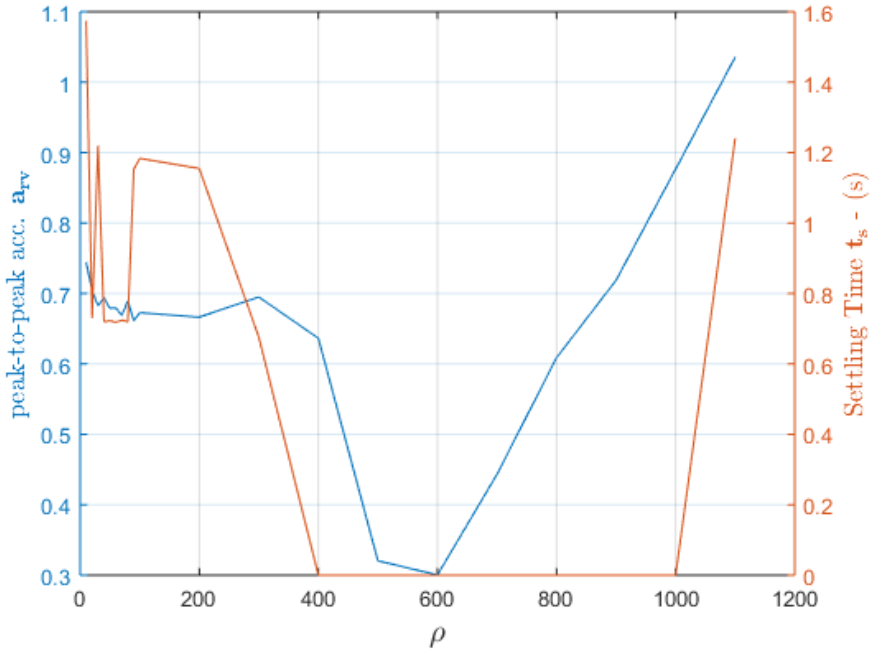

(a) No friction in the model-based part of the computed torque controller.

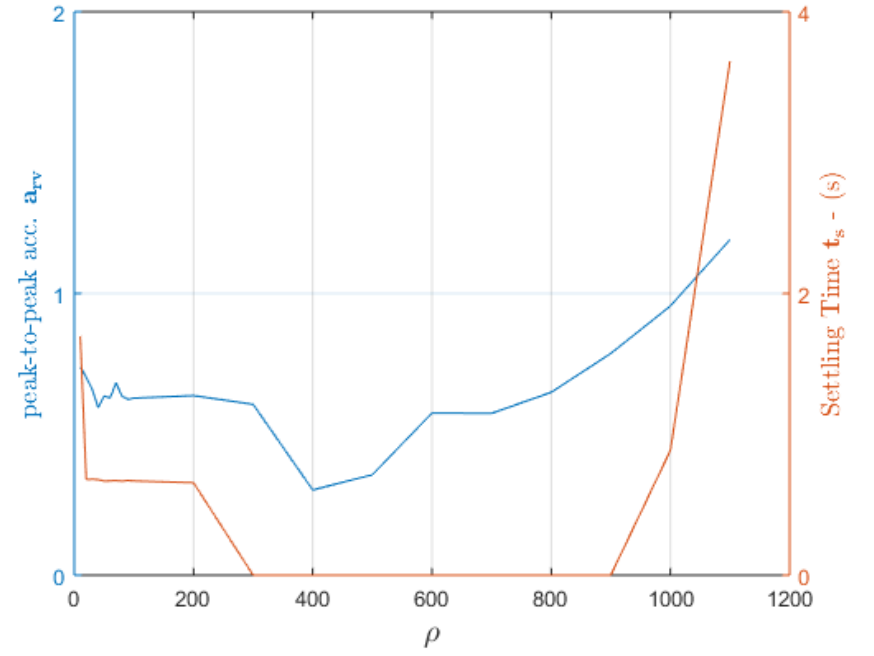

(b) Parameter mismatch between the model-based part and the plant.

Figure 4.3. Simulation results for different model parameter cases.

tion (3.33), and studying what demands the shaped input places on the actuators and how well it fares in its vibration performance considering identical levels of resonant energy in the input. These cases were constructed offline by plotting the variations of $F(\omega_{12})$ and Γ, as defined in Equations (3.13) and (3.14), against the weighting factor ρ and thereby selecting appropriate inputs for either fixed Γ or $F(\omega_{12})$, Figures 3.9 and 3.10.

Figures 4.4 to 4.11 show four different versine cases each for the closed-form approach and the numerical approach, for a move time of 2 seconds. V_{cf} and V_{num} denote the closed-form and numerical profiles for the versine. A similar notation is used for the ramped sinusoid, shown in Figures 4.12 to 4.19. Each figure shows the desired and actual motor angles, θ_3 and θ_4, the desired input acceleration, $\ddot{\theta}_{3,4,d}$, and its frequency spectrum, motor torques, T_1 and T_2 and the link accelerations, $\ddot{\theta}_{1,2}$.

In all of the experimental results, it can be seen that there are small steady-state errors in the tracking of motor trajectory, $\theta_{3,4}$. Since there is no integral term in the controller, these offsets are expected. It essentially results in the robot links not reaching the desired final position at times. However, the focus of this work lies in residual vibration reduction and the presence of these steady-state errors is secondary. An unshaped bang-bang, Figure 4.20, and an inverse kinematic profile, Figure 4.21, have also been considered as an alternate to the command shaped inputs. In general, most of the shaped profiles comfortably outperform either of these two alternate approaches. Note that for inverse kinematics, the residual acceleration is lower than all of the versine profiles, Table 4.1. This observation can be attributed to

the fact that inverse kinematic profiles are highly conservative and have minimal high frequency components, which leads to lower residual acceleration recordings but the position residuals and the settling times are both always poorer than either ramped sinusoid or versine profiles.

In Figures 4.4 and 4.5, it can be seen that for input profiles with maximum $\ddot{\theta}_{3,4,d}$ at $129\,rad/s^2$, the numerical form solution does not show spikes at transition between the nominal acceleration and deceleration phases and has a faster settling time than the counterpart in the closed-form method. Similar behavior can be observed using another Γ constrained case in Figures 4.6 and 4.7. It is important to note that in Figure 4.7, the commanded input $\ddot{\theta}_{3,4,d}$ is completely bounded in contrast to sharp degeneracies observed in closed-form profiles, Figures 4.6, 4.8 and 4.10. In the case with similar frequency attenuation $F(\omega_{12})$, Figures 4.8 and 4.9, an important observation is that performance of the two methods is more or less equal with settling time t_s of the order of 1.85 s. However, in the case of the numerical solution the demand put on actuators is considerably less, with peak acceleration in the input to be $29.13\,rad/s^2$ compared to $100.5\,rad/s^2$ for the analytical approach. Again, the difference can be clearly seen while looking at the bounded form of the input acceleration in Figure 4.9. This form qualitatively resembles a multi-switch bang bang solution as proposed by Meckl in [13]. However, this solution has not made use of any additional model information in generating the shaped command.

When looking at the influence of the weighting factor ρ, it is clear that in the range of considered cases, increasing ρ has consistently resulted in improved settling times.

However, the vibration amplitude has gone up in several cases, i.e., for V_{cf} $\rho = 1000$ to V_{cf} $\rho = 10000$. This can partly be attributed to larger high-frequency harmonics in case of V_{cf} $\rho = 10000$, which is confirmed by more spikes in the accelerometer signal. This behavior is not evident in case of the numerical-form solution for the versine.

Similar inferences can be drawn for the two approaches in case of ramped sinusoid profiles as well. For a fixed actuator limit or an upper bound on Γ_{RS}, the analytical solution performance is exceeded by the numerical approach, Figures 4.12 to 4.15. When looking at the Fourier plots of the shaped inputs, it can be noticed that, with increasing ρ, the troughs around the two natural frequencies get more pronounced and, hence, lead to larger peaks in the input. In general, the numerical-solution ramped sinusoid profile with $\rho = 1550$, Figure 4.19, achieves the least residual oscillations and also the input profiles are fairly moderate in ampltidue.

The ramped sinusoid, like the versine, shows spikes during transit from acceleration to deceleration phase. However, for the ramped sinusoid, these peaks are much higher and, for safety reasons, the driving torque for the second motor in Figure 4.18 was saturated. The effect of saturation can be seen in imperfect trajectory tracking. This further strengthens the need to avoid degenerate trajectory profiles that require oversized actuators. A bounded numerical-form solution does not compromise on performance, at the same time generating moderate input trajectories, which avoid the need for supplying high torques intermittently and thus proving to be more efficient. Removing the Gibbs effect in approximation of the bang bang, therefore, results in inputs that more effectively use the available torque without negatively impacting

the performance. These results further corroborate the findings in Chapter 3, where it was concluded that uniform convergence of coefficients results in better utilization of available energy and improves performance of the shaped profiles.

Table 4.1. Residual vibration performance of Versine profiles.

Comparison Basis	**Profile**	ρ	Δ_{xy} (rad)	a_{rv} (m/s^2)	t_s (s)	$\ddot{\theta}_{d,max}$ (rad/s^2)
$20.9 \leq \Gamma_v \leq 21.7$	V_{cf}	1000	0.0454	0.7917	1.0130	129.8
	V_{num}	10000	0.0332	0.7921	0.9755	125.6
$29.6 \leq \Gamma_v \leq 30.1$	V_{cf}	2000	0.0458	0.9788	1.764	180.1
	V_{num}	15000	0.0333	0.7904	0.8805	177.6
Scaled Magnitude *=9.68 dB*	V_{cf}	500	0.0452	0.8080	1.8550	100.5
	V_{num}	1250	0.0437	0.7811	1.8435	29.13
Scaled Magnitude *=8.16 dB*	V_{cf}	10000	0.0251	1.0130	0.8200	354.4
	V_{num}	25000	0.0201	0.7300	0.8000	276.3
	Bang-Bang		0.2337	2.1068	3.8420	6
	Inverse Kinematics		0.0616	0.6198	1.9355	16.45

Table 4.2. Residual vibration performance of Ramped Sinusoid profiles.

Comparison Basis	**Profile**	ρ	Δ_{xy} (rad)	a_{rv} (m/s^2)	t_s (s)	$\ddot{\theta}_{d,max}$ (rad/s^2)
$3.47 \leq \Gamma_{RS} \leq 3.5$	RS_{cf}	1.5	0.0424	0.8515	0.9260	75.59
	RS_{num}	141	0.0116	0.8016	0.7715	72.65
$4.99 \leq \Gamma_{RS} \leq 5$	RS_{cf}	16	0.0110	0.4915	0.7575	149.7
	RS_{num}	2900	0.0045	0.3902	0.4040	152.8
Scaled Magnitude *=1.741 dB*	RS_{cf}	56	0.0108	0.4825	0.8575	194.6
	RS_{num}	96	0.0085	0.7311	0.6175	69.37
Scaled Magnitude *=0.1 dB*	RS_{cf}	900	0.0164	0.7436	0.8305	**796.1**
	RS_{num}	1550	0.0041	0.1786	0.1645	113.1
	Bang-Bang		0.2337	2.1068	3.8420	6
	Inverse Kinematics		0.0616	0.6198	1.9355	16.45

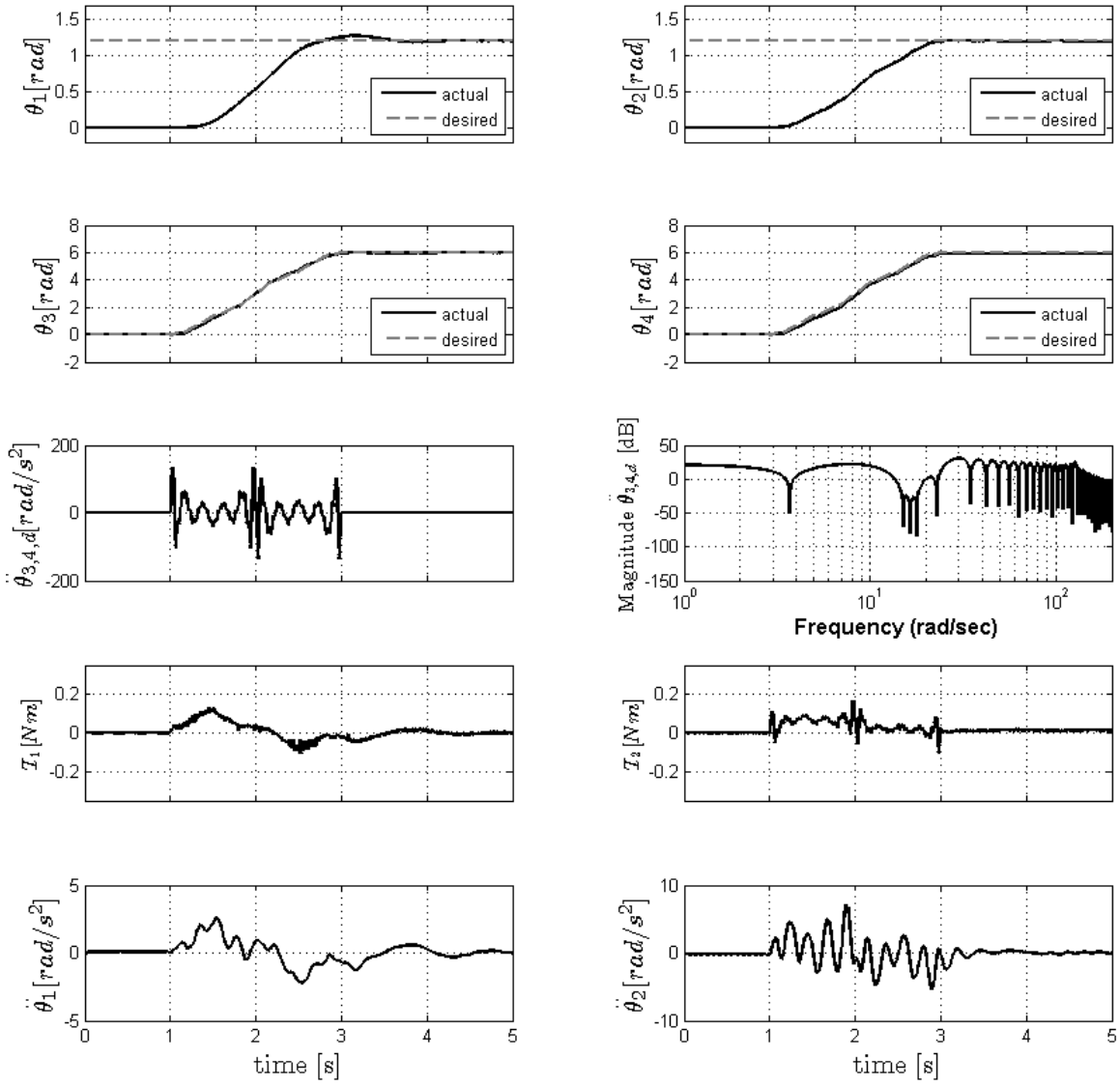

Figure 4.4. Experimental result for closed-form versine with ρ=1000.

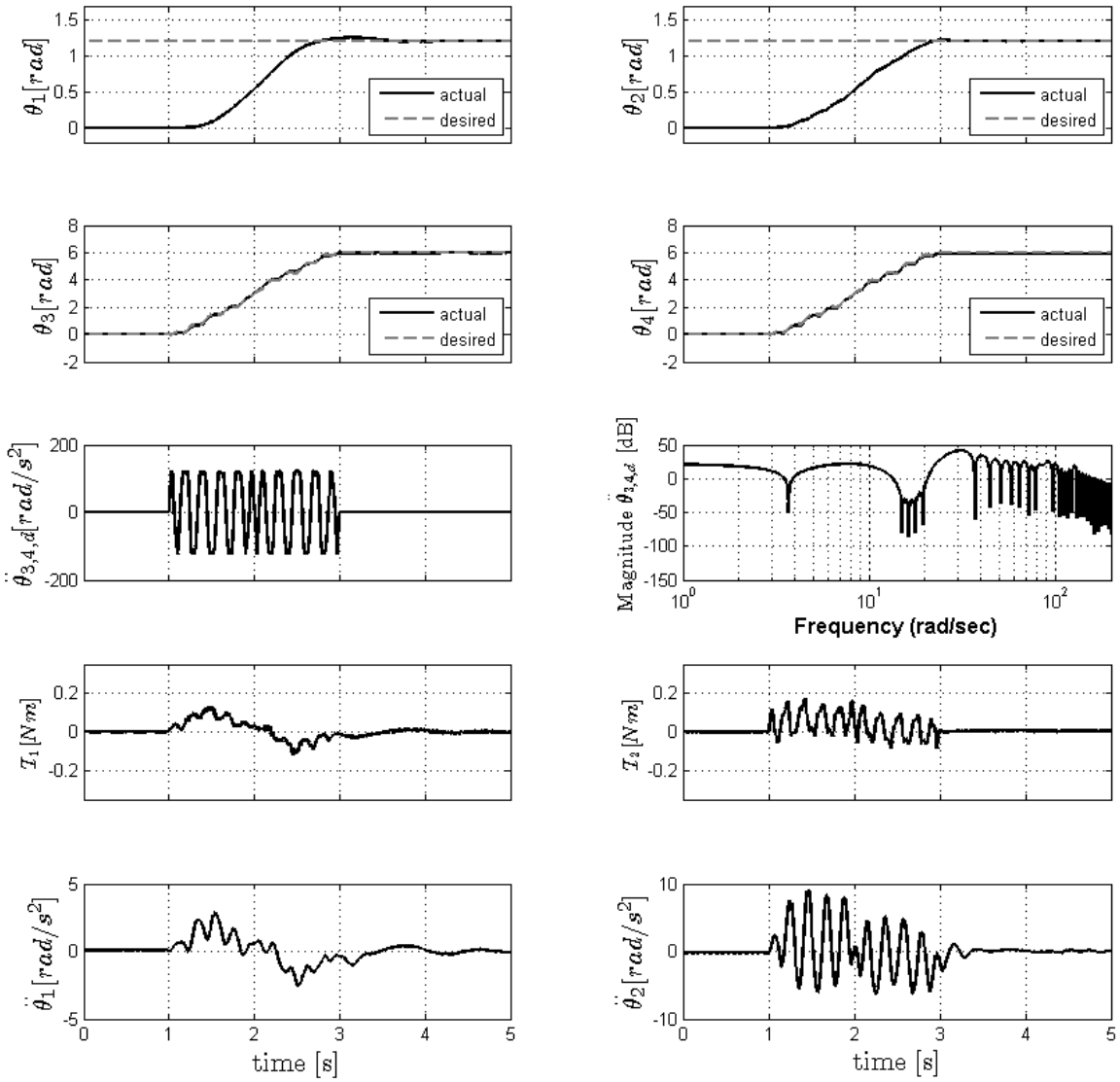

Figure 4.5. Experimental result for constrained numerical-form versine with ρ=10000.

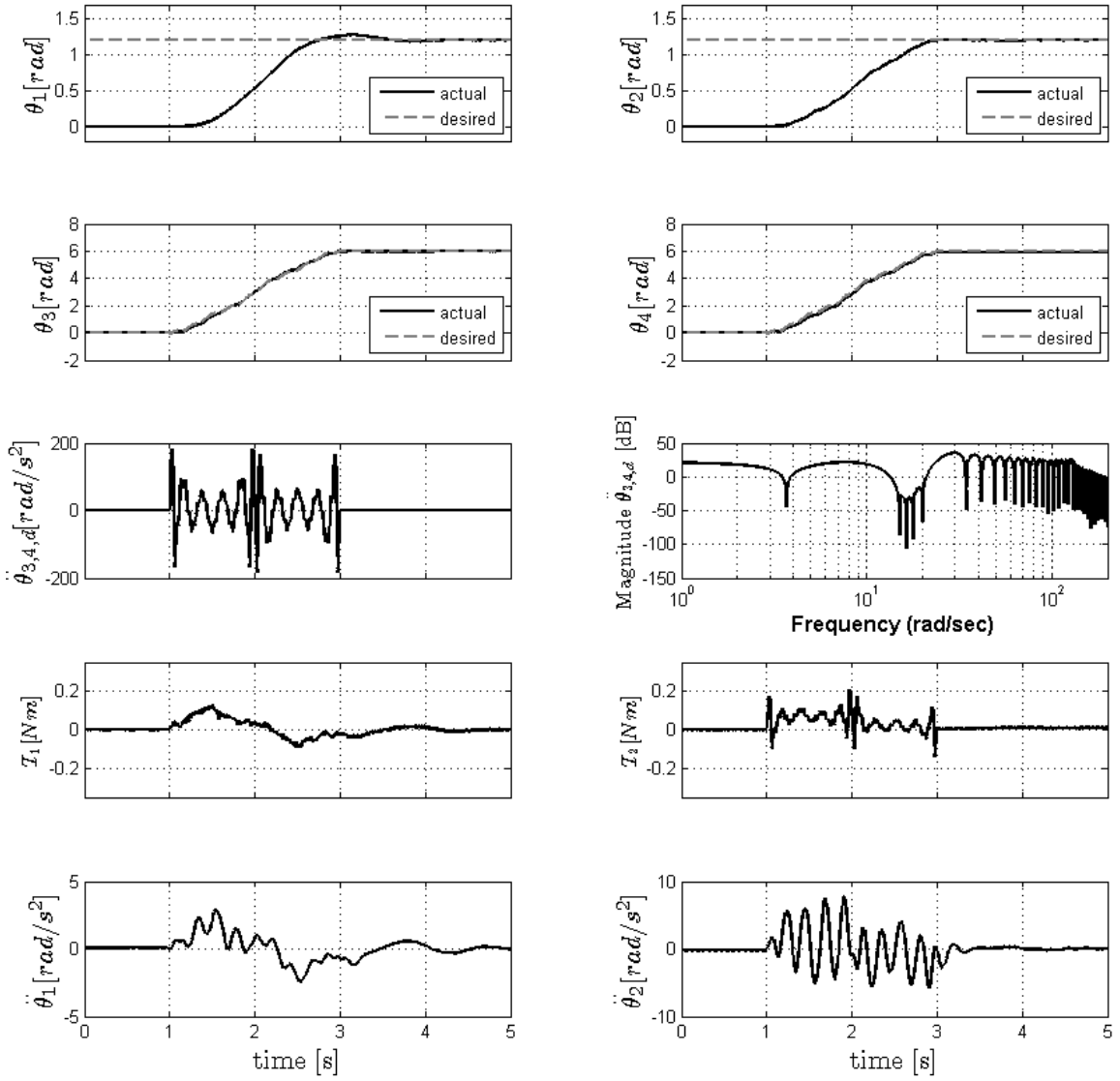

Figure 4.6. Experimental result for closed-form versine with ρ=2000.

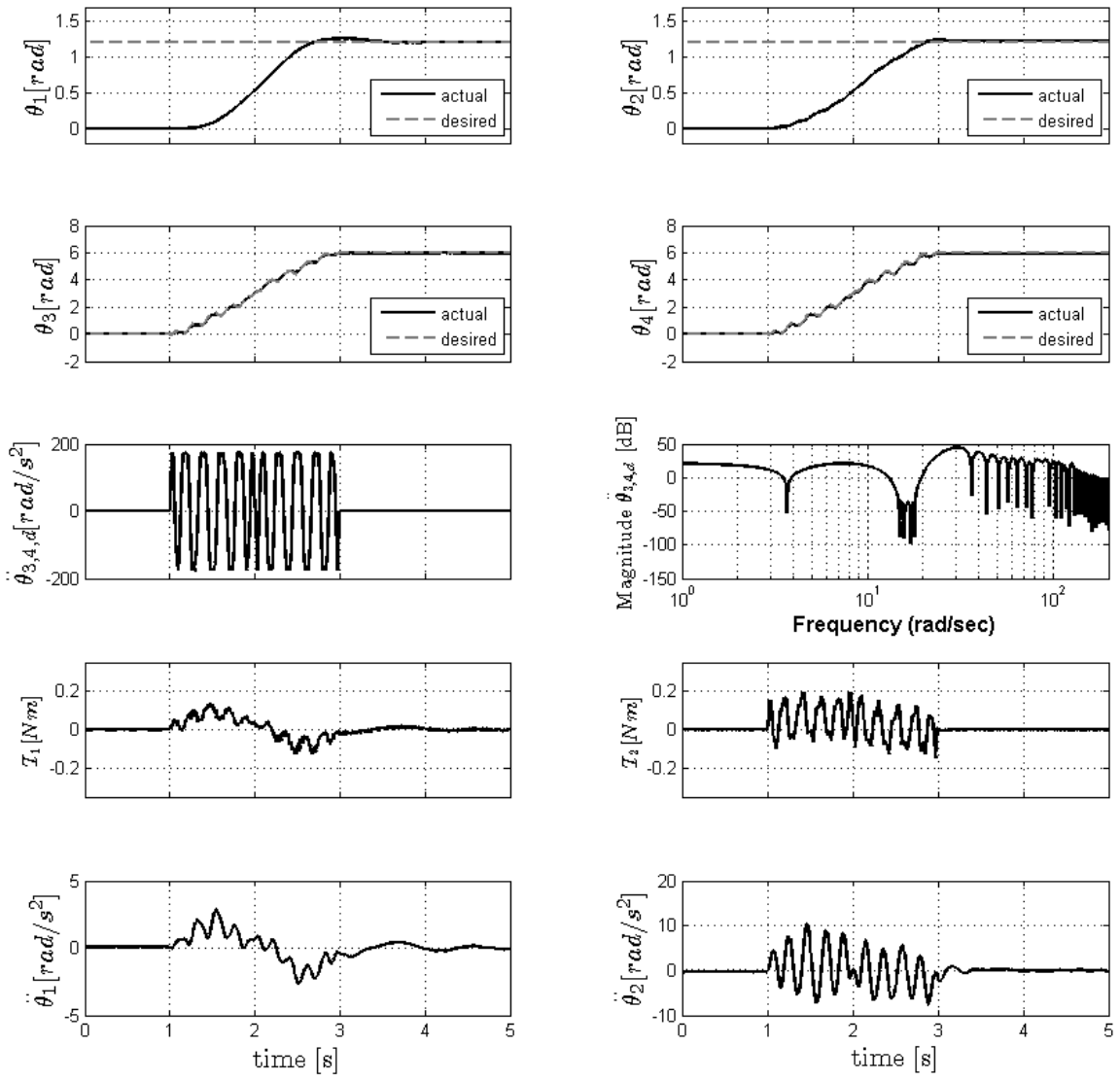

Figure 4.7. Experimental result for constrained numerical-form versine with ρ=15000.

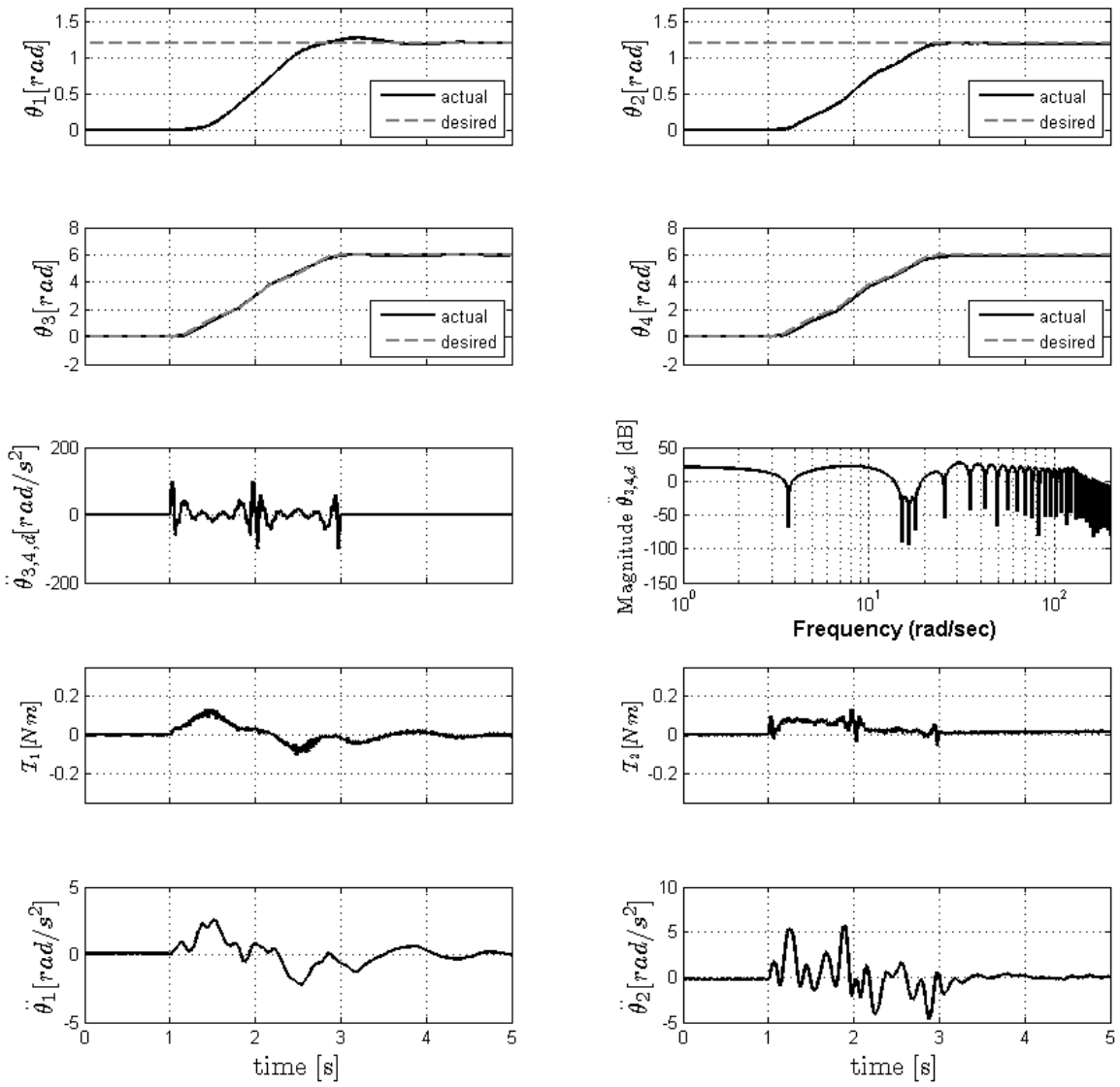

Figure 4.8. Experimental result for closed-form versine with ρ=500.

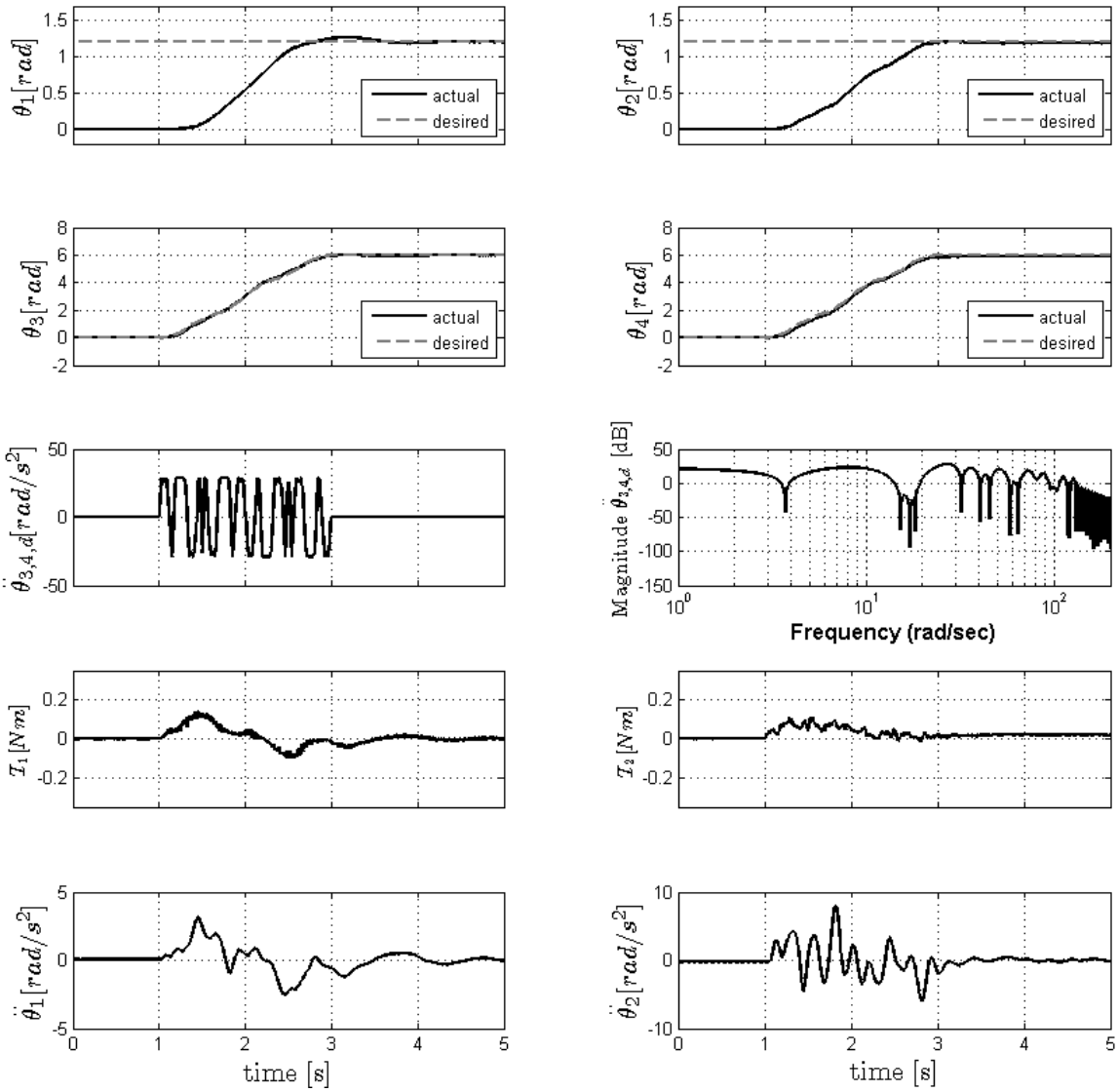

Figure 4.9. Experimental result for constrained numerical-form versine with ρ=1250.

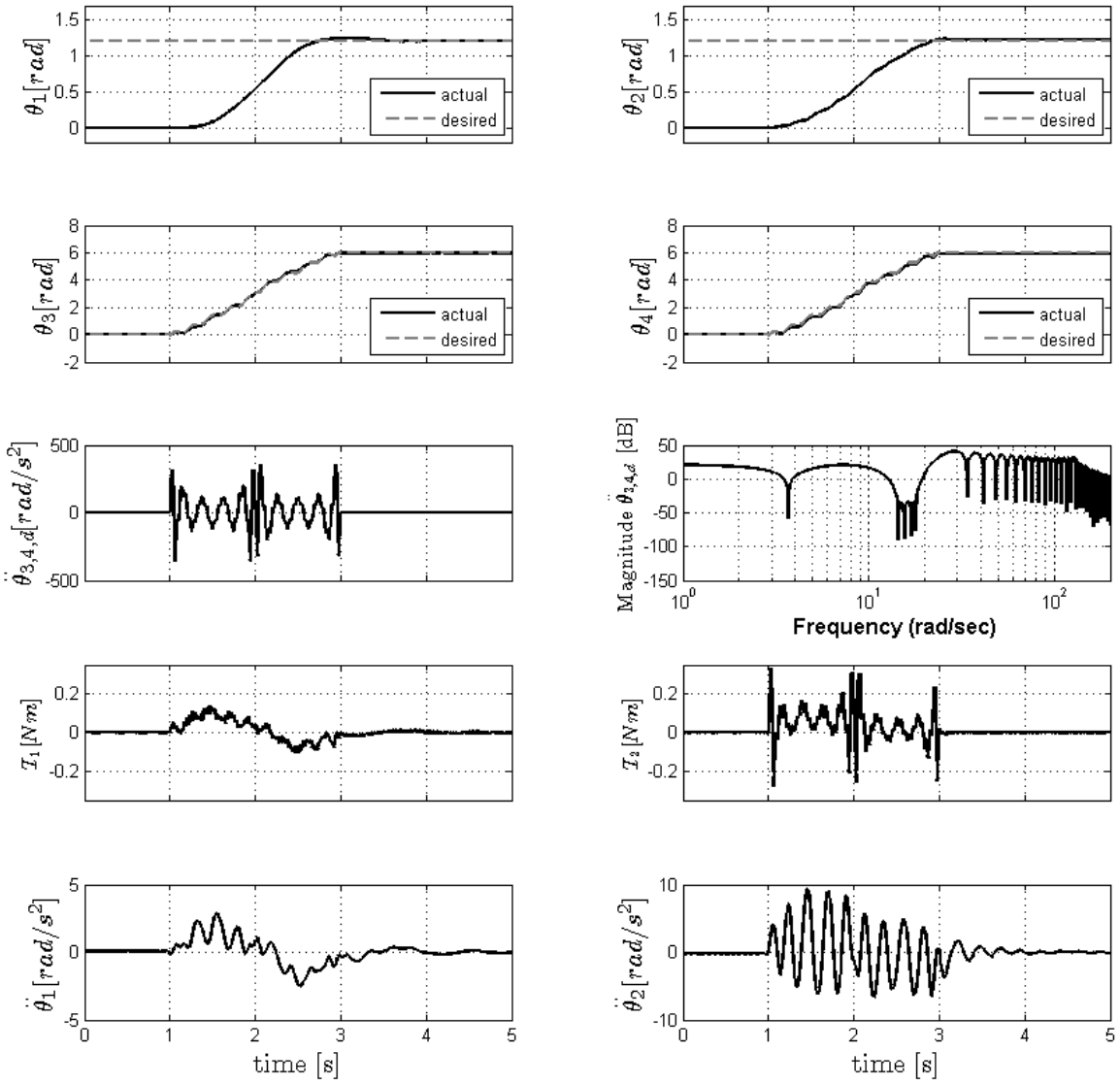

Figure 4.10. Experimental result for closed-form versine with ρ=10000.

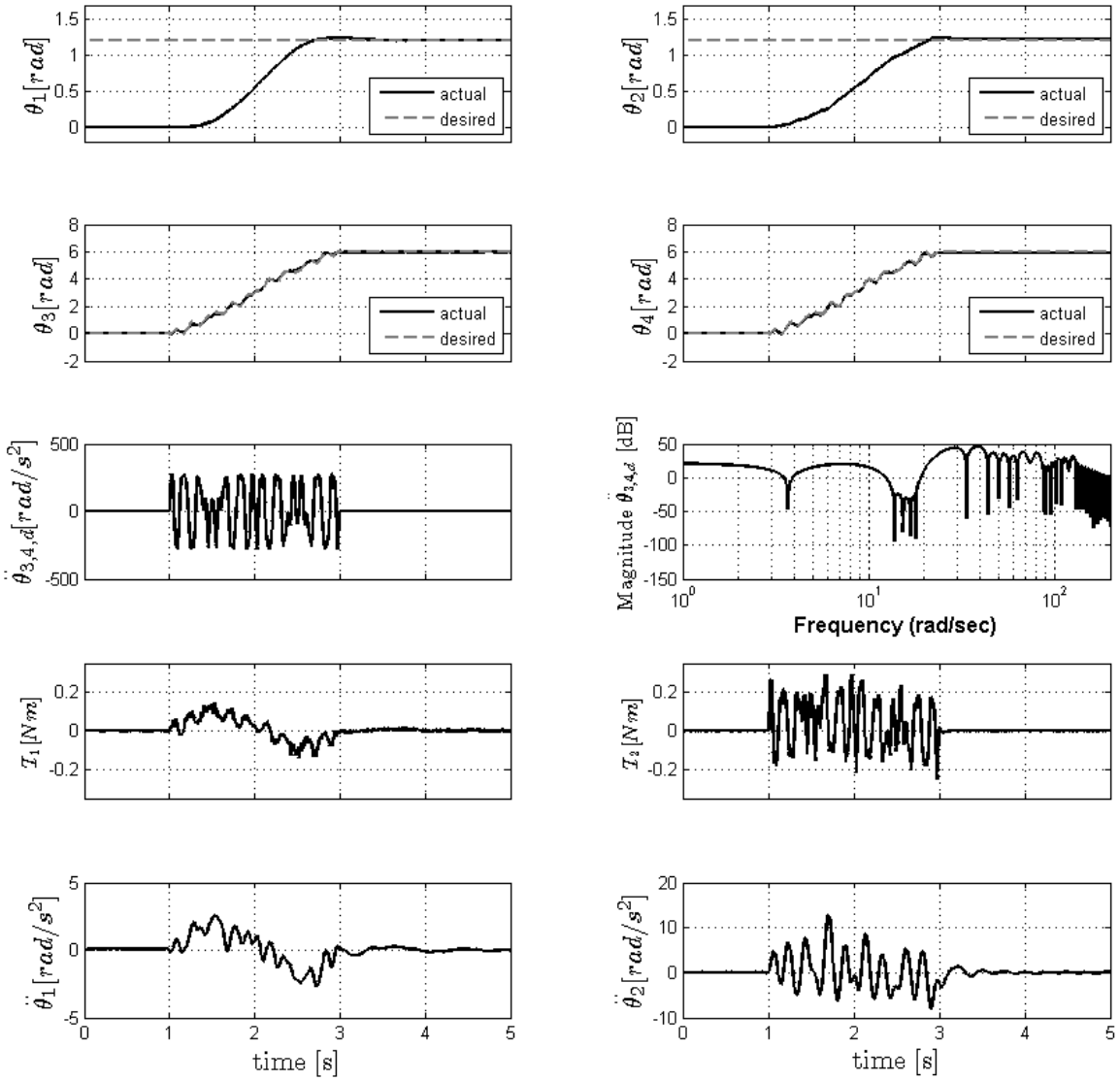

Figure 4.11. Experimental result for constrained numerical-form versine with ρ=25000.

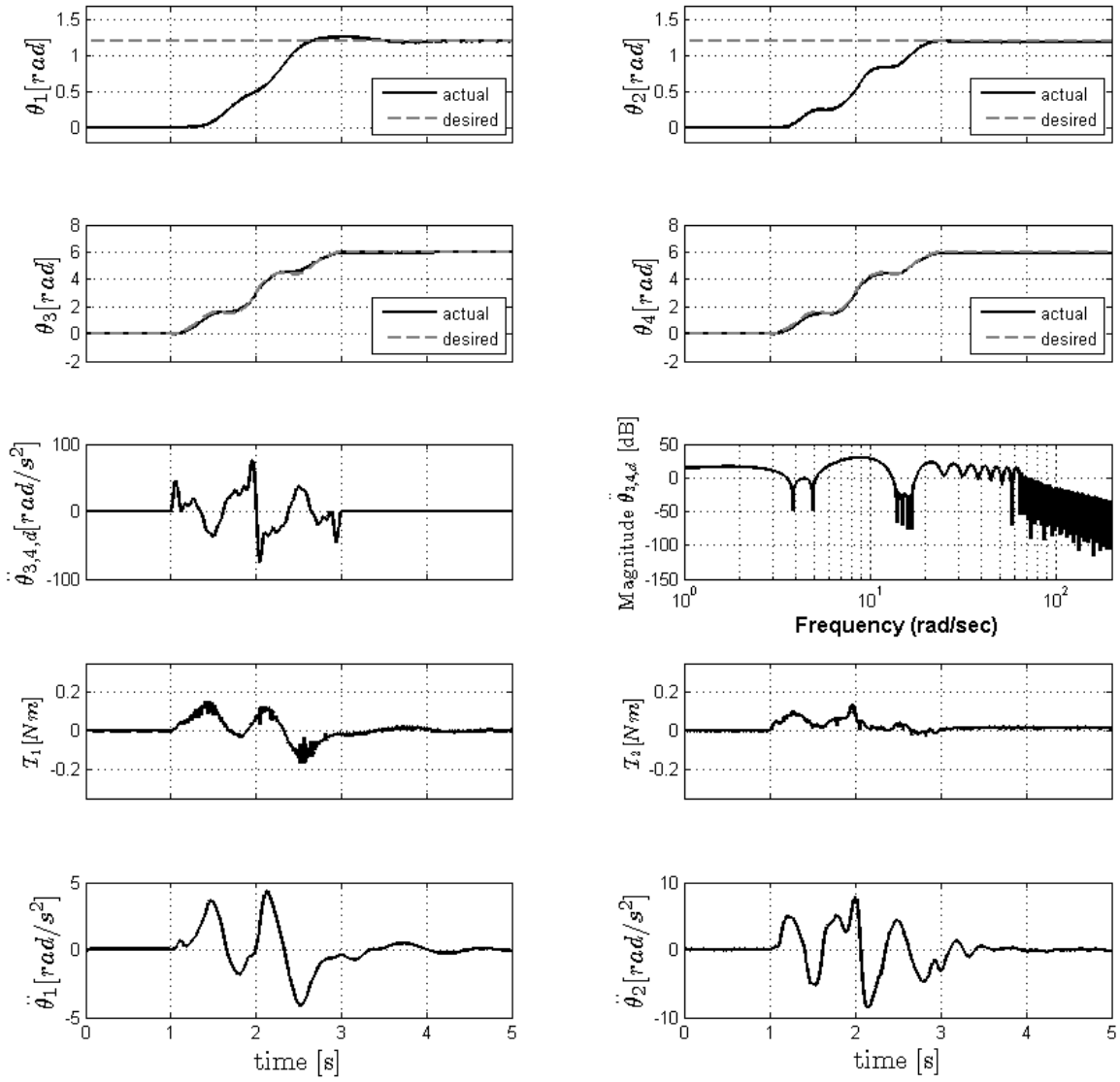

Figure 4.12. Experimental result for closed-form ramped sinusoid with ρ=1.5.

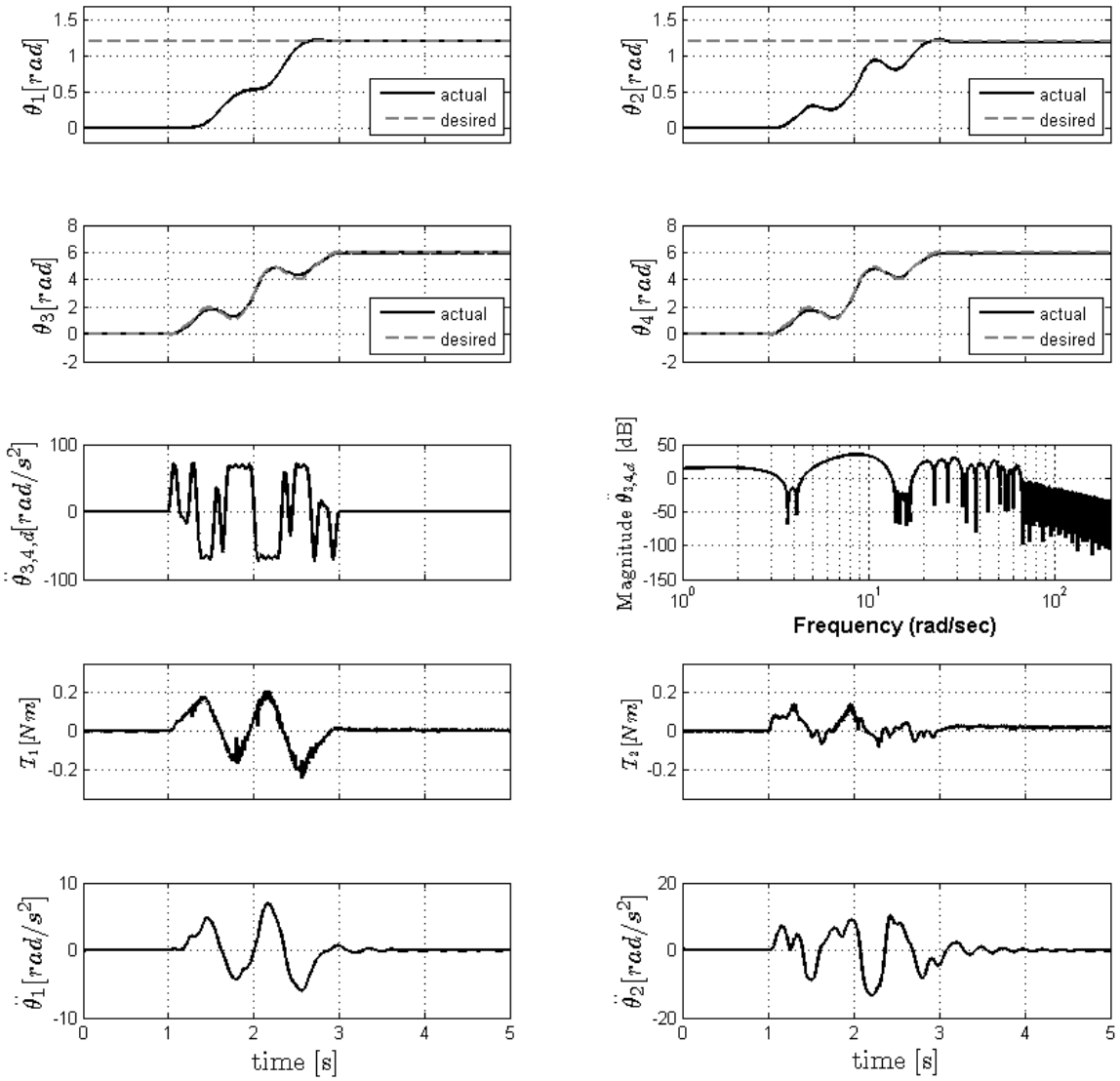

Figure 4.13. Experimental result for constrained numerical-form ramped sinusoid with ρ=141.

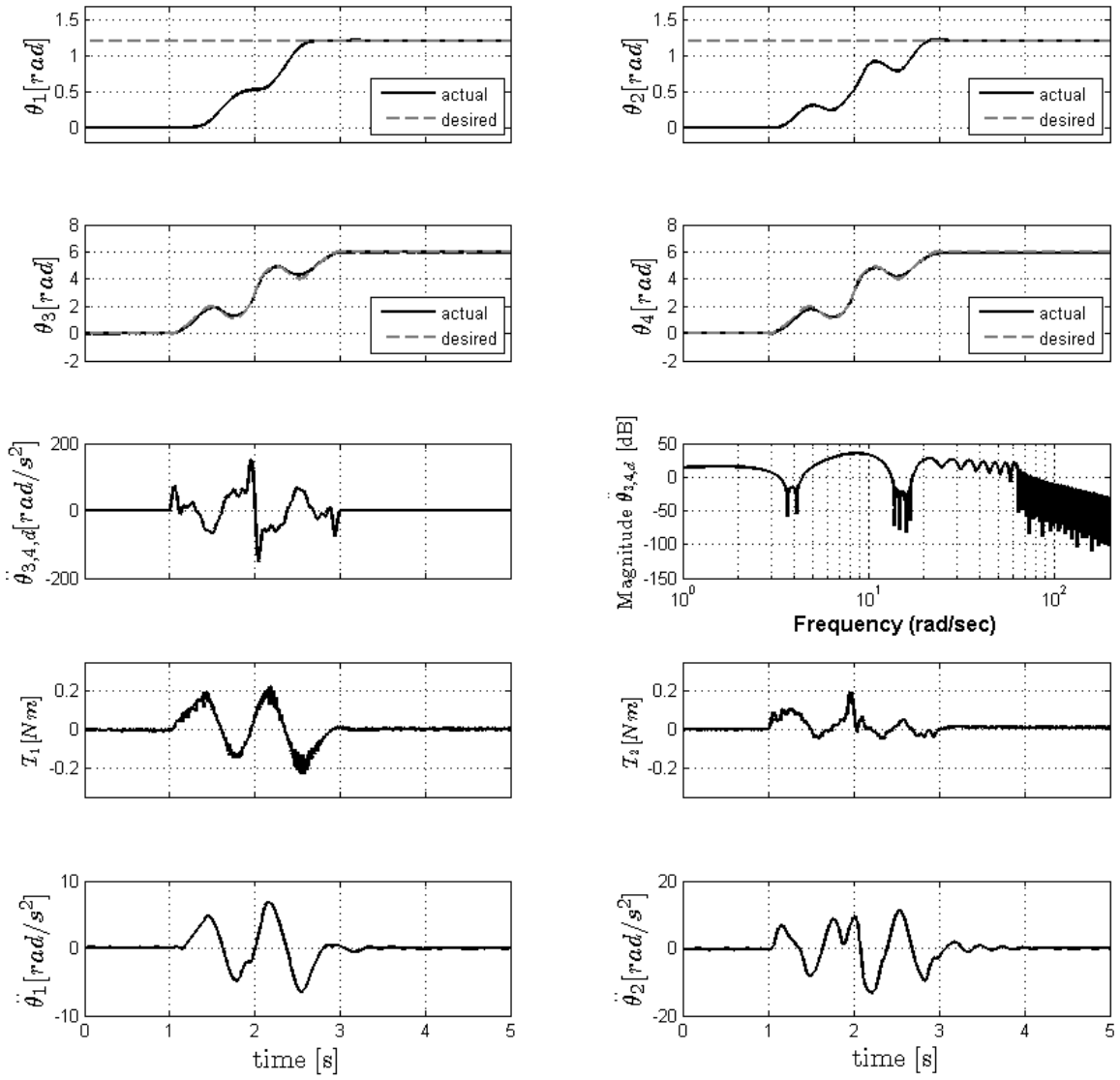

Figure 4.14. Experimental result for closed-form ramped sinusoid with ρ=16.

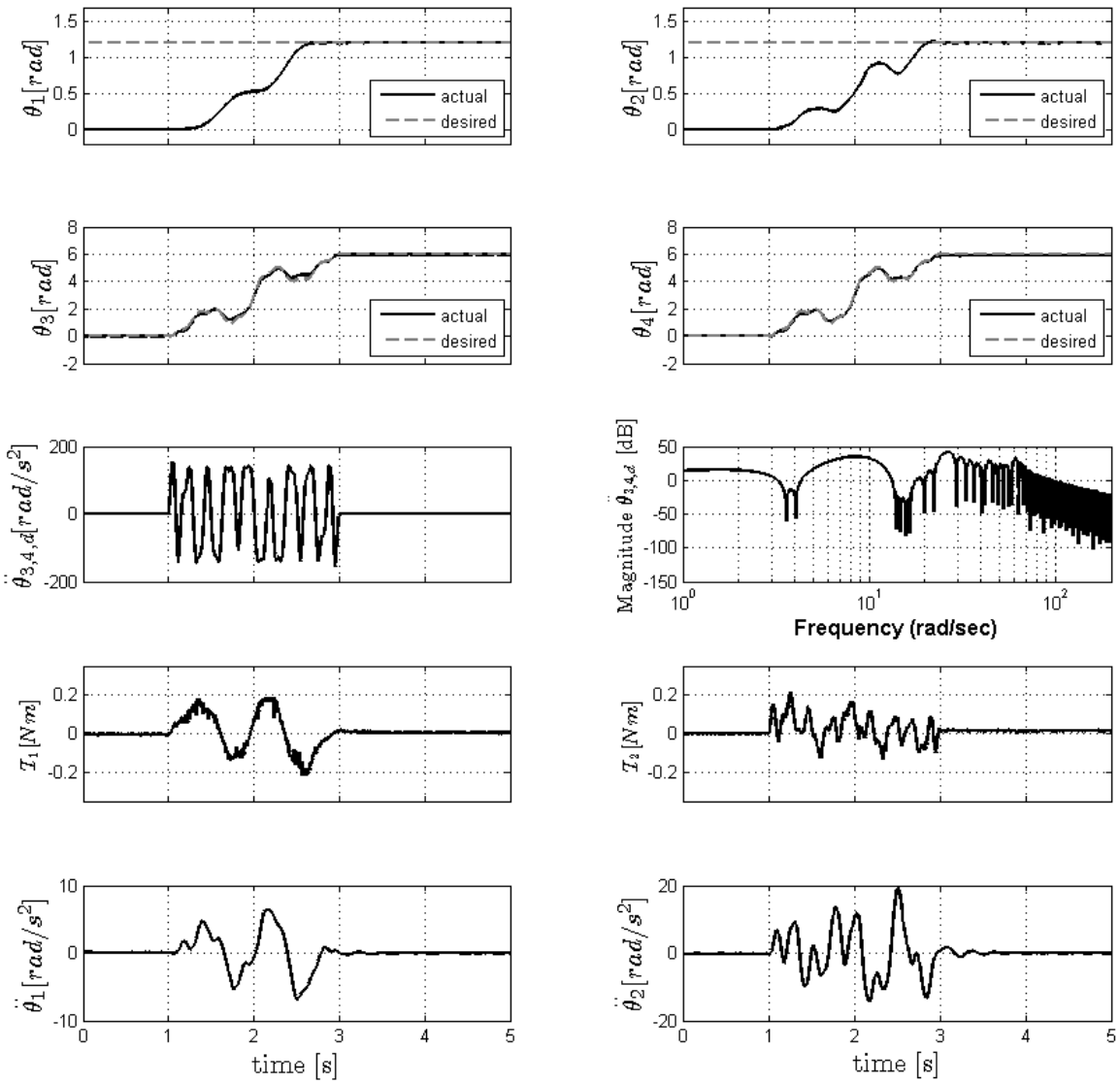

Figure 4.15. Experimental result for constrained numerical-form ramped sinusoid with ρ=2900.

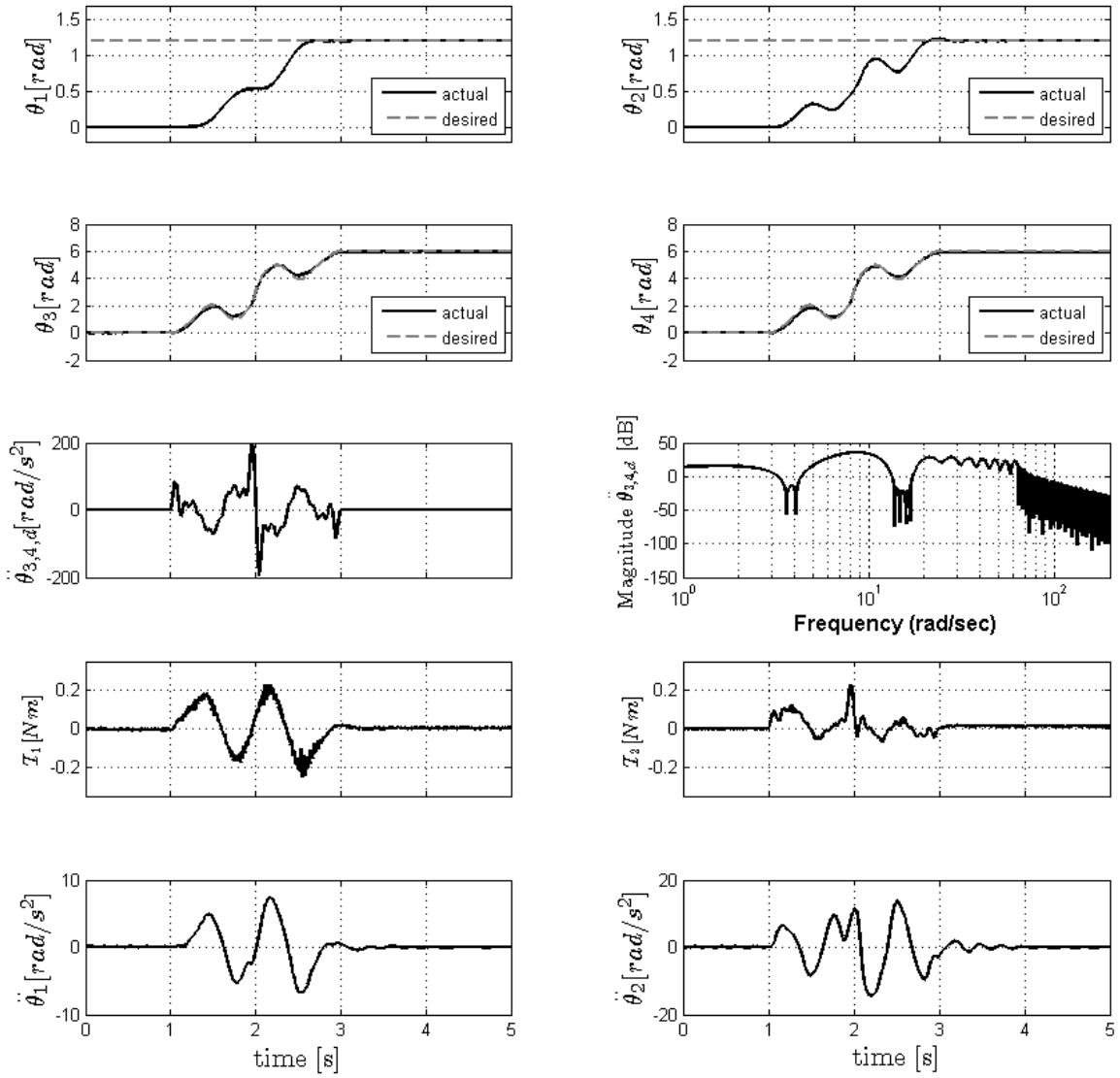

Figure 4.16. Experimental result for closed-form ramped sinusoid with ρ=56.

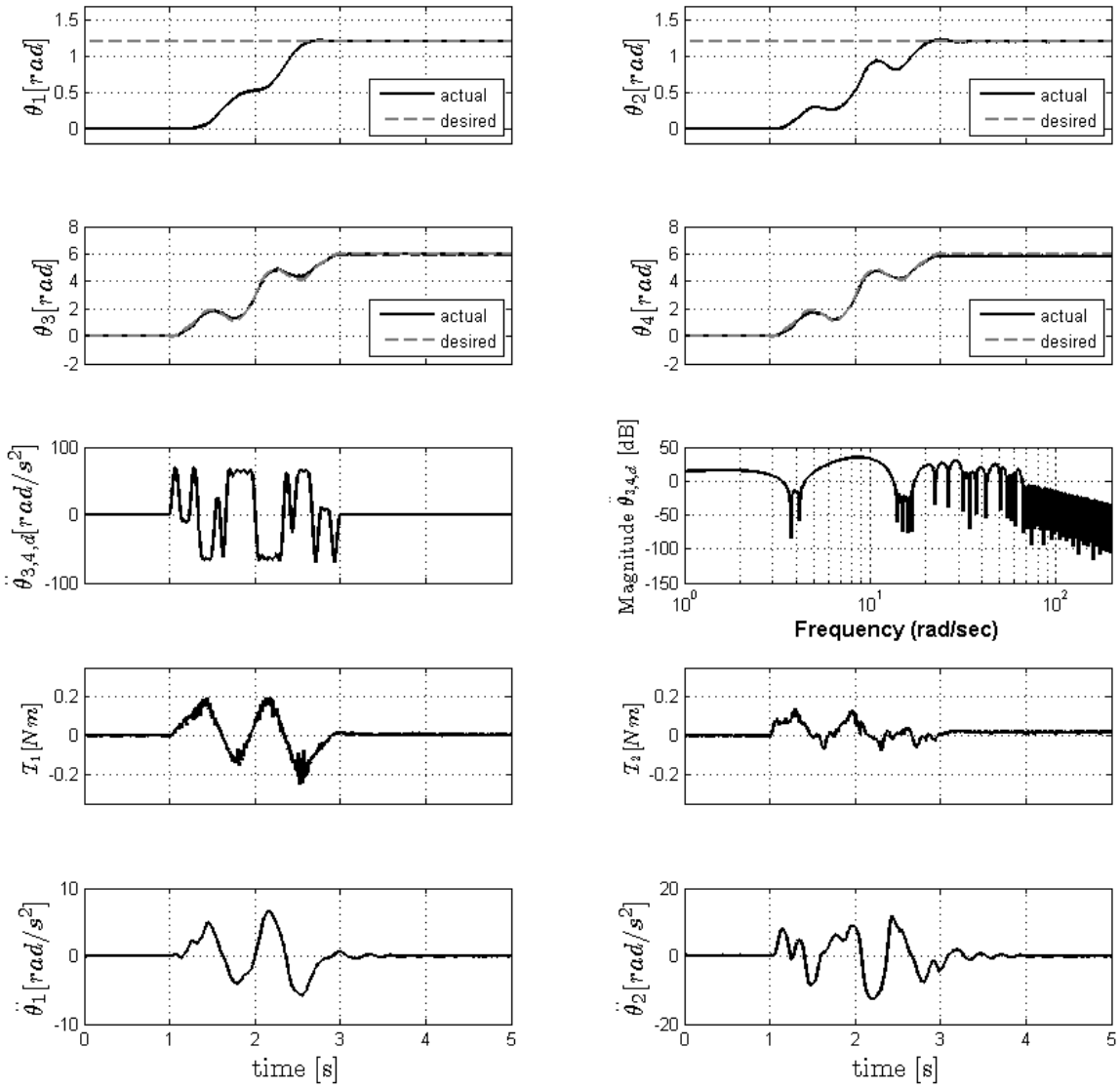

Figure 4.17. Experimental result for constrained numerical-form ramped sinusoid with ρ=96.

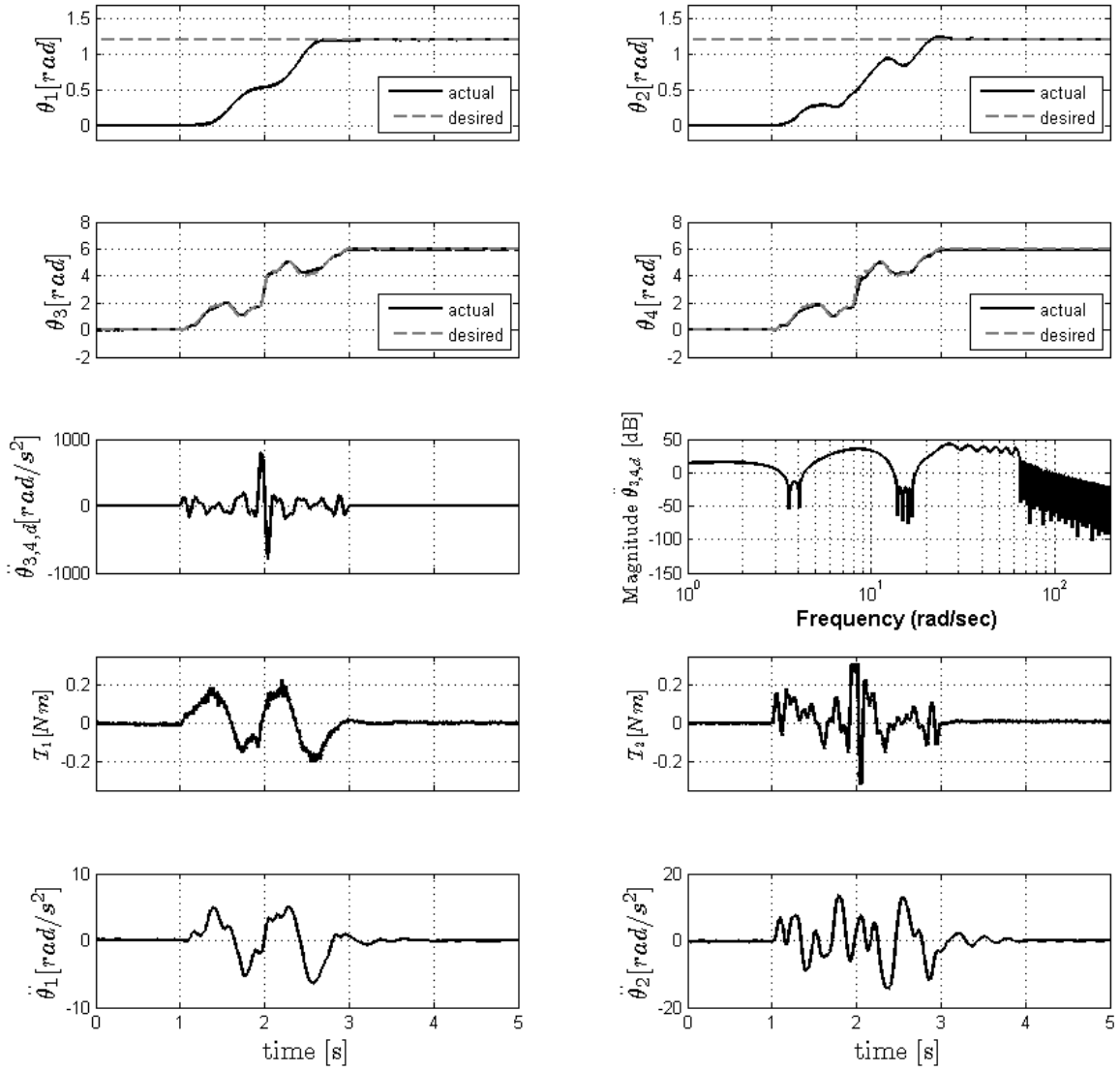

Figure 4.18. Experimental result for closed-form ramped sinusoid with ρ=900.

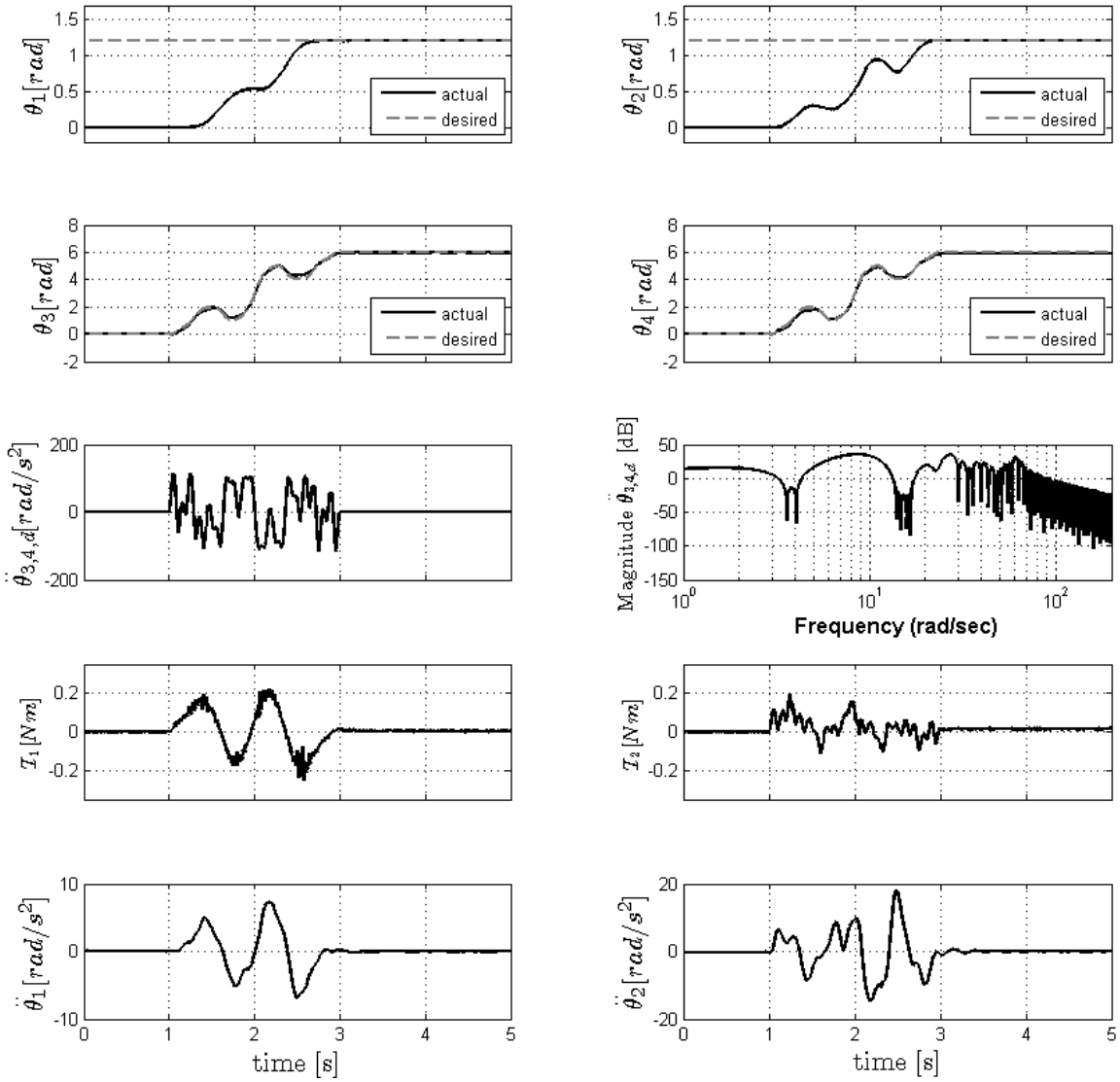

Figure 4.19. Experimental result for constrained numerical-form ramped sinusoid with ρ=1550.

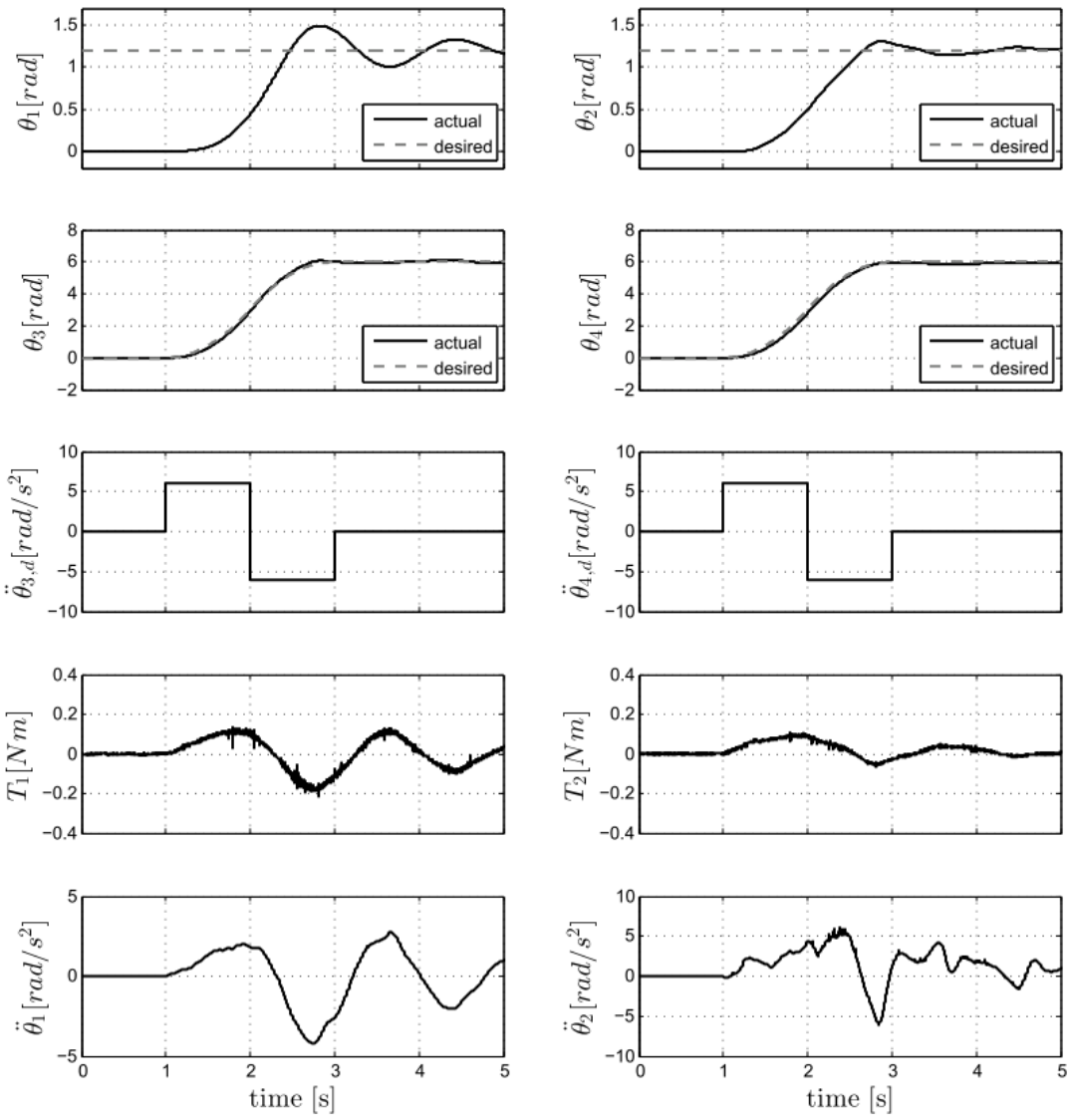

Figure 4.20. Experimental result for an unshaped bang-bang profile.

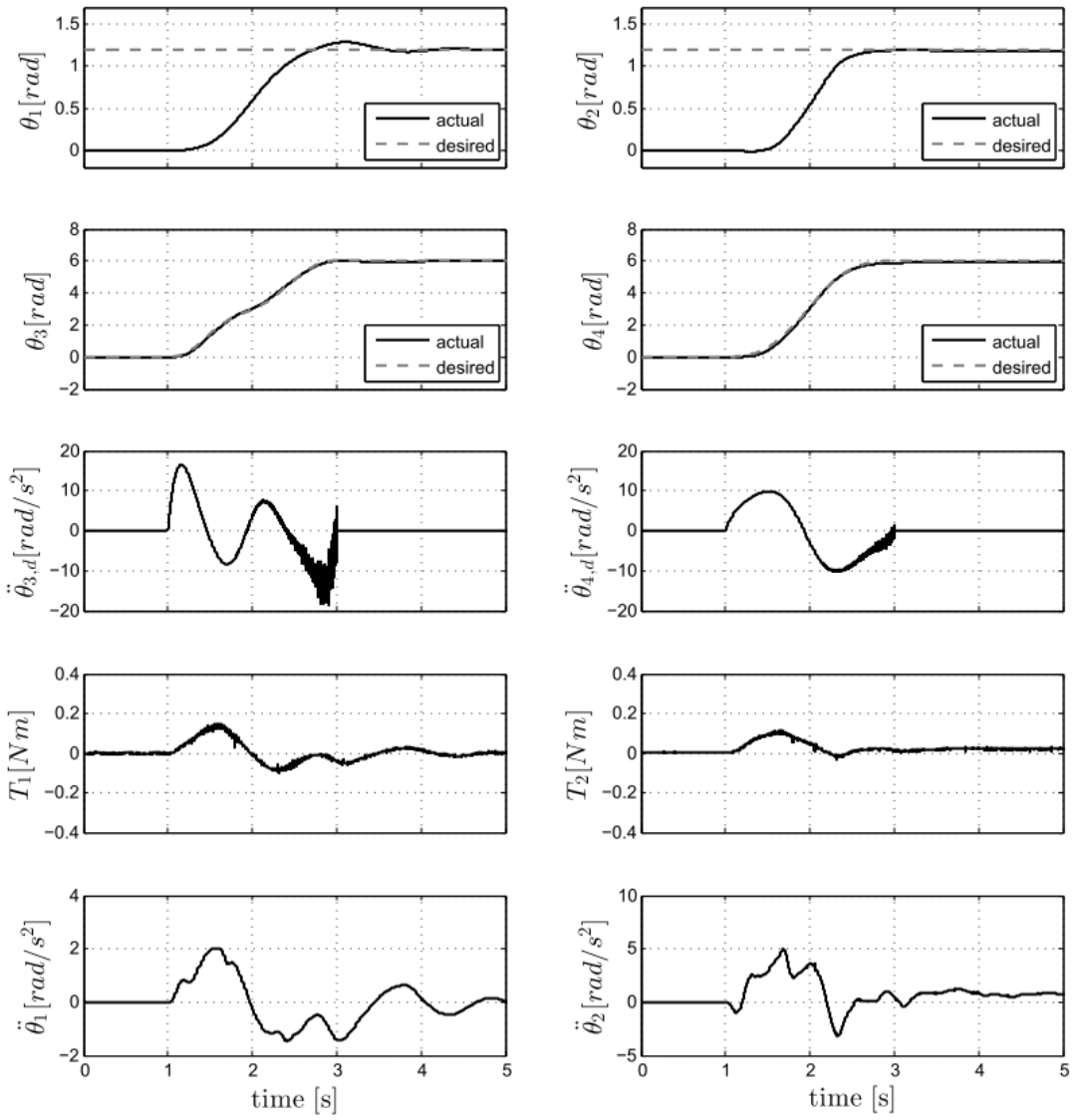

Figure 4.21. Experimental result for an inverse kinematics profile.

5. CONCLUSIONS AND RECOMMENDATIONS

5.1 Summary and Conclusions

In this work, the command shaping approach has been extended in the form of a constrained numerical optimization problem. The Gibbs effect that occurs for discontinuous function approximation inherent to the command shaping technique is studied. Possible causes for the ringing artifacts in the approximated function were identified and, more importantly, their implications to the design of command inputs was studied. Through simulations for design of commanded profiles, the tradeoff between critical energy attenuation and error in fit to the time-optimal bang-bang function was explored. It was found that with L_2-norm approximations of the bang-bang reference, when the detrimental resonant energy is attenuated in the inputs, the redistribution of energy takes place in a manner such that more energy gets pumped into the blips that are present due to the Gibbs phenomenon. Because of this, as more attenuation was sought, the peaks in the input took even higher values with sharp spikes at the discontinuity.

After demonstrating the ill-effects of the undesired oscillations around the jump discontinuity, a constrained numerical approach was introduced to obtain the L_1-norm approximation of the square wave cycle for both the versine and the ramped sinusoid functions. It was observed that the numerical L_1-norm generates much smoother

approximations, even at the discontinuity, and leads to faster decay of harmonic coefficients and more uniform convergence across the period of the bang-bang. And when the resonant frequency content is penalized, the energy is now redistributed to intermediate modes in a manner that keeps the acceleration profiles bounded without sacrificing attenuation performance. By observing the payback between the two competing objectives of the cost function, the variations of maximum input acceleration demand on the actuator and the flexible mode energy were simultaneously analyzed against an increasing weighting factor on frequency attenuation, ρ. It was observed that, beyond a point in the solution space, the error of fit to the bang-bang function starts dominating the penalty on frequency, and the solution ventures into regions that are suboptimal with respect to both objectives. Therefore, by exploring this multiobjective interaction, a method has been outlined to select ρ based on profile characteristics. Although the proposed numerical approach is computationally more expensive, since the commands are generated offline, it does not prove to be a limiting factor. The numerical-form solution provides more flexibility in formulating the optimization problem, with a scope of including nonlinear constraints to control the generated input to have certain attributes, such as imposing a direct limit on maximum permissible torque demand or controlling the frequency content to a specific amount, which then directly governs the performance of simple linear systems.

After demonstrating the useful tradeoffs that occur in the numerical approach, the generated inputs for both approaches were applied in experiments to the two-link robot platform. To critically evaluate the performance of different inputs, several

important metrics were defined to obtain a better sense of vibrations in the response. Measures of settling time and peak-to-peak planar residual acceleration were able to capture the vibration in the system. However, for complete comparison between different inputs, more than one metric has to be considered. One single metric could not effectively combine both the vibration amplitude and the dissipation performance. The standard closed-form technique for command shaping, as discussed in section 3.1, was experimentally compared to the numerical approach. The formulated numerical solution showed superior residual vibration performance for a given limit on maximum input acceleration. Also, for this approach, a desired attenuation at the natural frequency posed less demands on the actuators by generating moderate input accelerations. The main feature behind a smooth fit to the bang-bang function and removing the Gibbs effect is that the generated input now more effectively utilizes the available energy with the maximum available torque. However, one needs to bear in mind that the redistribution of energy that occurs in the numerical approach could potentially excite any intermediate unmodeled modes. So, a careful analysis of existence of any such phenomenon is required to successfully use the technique.

5.2 Unique Contributions

There were multiple new findings from this work that warrant repeating. The primary contribution of this work was to develop a method that takes care of degeneracy in the shaped input profiles. The other benefits of this development were a closer exploration of the multiobjective cost function and how the factor ρ should be

best selected. Also, a framework has been put in place where the decision variables, i.e., the coefficients of harmonics of the basis function, can now be manipulated with greater flexibility, wherein the nature of inputs can be constrained more directly. Another development was inclusion of the accelerometer response in the experimental analysis. Using accelerometer data, multiple single-parameter metrics were defined for estimating the vibration performance. It was pointed out that due to the coupling and interaction between the two modes of the system, the focus should shift to looking at only the end-effector vibration rather than vibration of each link.

There were other developments that although not instrumental in meeting the core objective, nevertheless proved significant. It was discovered that the simulation model needs more fine tuning to build in appropriate mismatch between the model-based part of the controller and the robot plant, to obtain results or trends that better match experimental results.

5.3 Recommendations for Future Work

One area that could be explored in the future is to extend the proposed optimization model to consider the simulated vibration performance in defining the fitness function. Inputs can be designed directly with the objective of minimizing residual vibration in simulation response, subjected to desired move times or actuator size constraints. In addition, the interaction and the effect of multiple modes in light of frequency attenuation at each mode needs further inspection. In the current work, both modes are equally weighted for attenuation, but a simple two-mode linear sys-

tem could be explored to begin with, to determine better ways of achieving uniform attenuation at each mode. Moreover, the basis for selection of ρ values could be studied further in parallel with determining appropriate scaling of Fourier magnitude at the two modes that can relate to vibration performance with more accuracy. One significant area of future work is to look at the effect of the computed torque controller on the shaped profile and if or how it shifts the points of attenuation in the frequency spectrum of the input to the robot.

The differences between maximum attainable attenuation for the ramped sinusoid and versine inputs should be inspected further. The attenuation window can be dialed in more carefully depending on the specific change in configuration of the robot for each segment. Moreover, the choice of number of harmonics should be investigated to ensure if we could add more power to the signal at the same time improving on attenuation performance. In addition, the possibility of determining the natural frequency of the system under varying payloads online could be explored.

LIST OF REFERENCES

LIST OF REFERENCES

[1] M. C. Readman. *Flexible Joint Robots*. CRC Press, Boca Raton, FL, 1994.

[2] S. F., N. Kyura, and S. Hara. Vibration absortion control of industrial robots by acceleration feedback. *IEEE transactions on Industrial Electronics*, 30:299–305, 1983.

[3] L. M. Sweet and M. C. Good. Re-Definition of the Robot Motion Control Problem: Effects of Plant Dynamics, Drive System Constraints, and User Requirements. In *Proceedings of the 23rd Conference on Decision and Control*, pages 724–732, Las Vegas, NV, 1984.

[4] P. Tomei. A Simple PD Controller for Robots with Elastic Joints. *IEEE Transactions on Automatic Control*, 36(10):1208–1213, 1991.

[5] L. Tian and A. A. Goldenberg. Robust adaptive control of flexible joint robots with joint torque feedback. In *Robotics and Automation, 1995. Proceedings., 1995 IEEE International Conference on*, volume 1, pages 1229–1234 vol.1, Nagoya, Japan, May 1995.

[6] H. Moulin and E. Bayo. On the Accuracy of End-Point Trajectory Tracking for Flexible Arms by Noncausal Inverse Dynamic Solutions. *J. Dyn. Sys., Meas., and Control*, 113:320–324, 1991.

[7] J. Ghosh and B. Paden. Pseudo-inverse based iterative learning control for nonlinear plants with disturbances. In *Decision and Control, 1999. Proceedings of the 38th IEEE Conference on*, volume 5, pages 5206–5212. IEEE, 1999.

[8] C. L. Lin and Y. H. Hsiao. Adaptive feedforward control for disturbance torque rejection in seeker stabilizing loop. *Control Systems Technology, IEEE Transactions on*, 9(1):108–121, 2001.

[9] C. Lewin. Motion control gets gradually better. *Machine Design*, 66(21):90–94, 1994.

[10] O. J. M. Smith. Posicast control of damped oscillatory systems. *Proceedings of the IRE*, 45(9):1249–1255, Sept 1957.

[11] N. C. Singer and W. P. Seering. Preshaping command inputs to reduce system vibration. *ASME Journal of Dynamic Systems, Measurement, and Control*, 112:76–82, 1990.

[12] S. P. Bhat and D. K. Miu. Precise point-to-point positioning control of flexible structures. *Journal of Dynamic Systems, Measurement, and Control*, 112(4):667–674, 1990.

[13] P. H. Meckl. *Minimizing Residual Vibration of a Linear System Using Appropriately Shaped Forcing Functions*. Master's thesis, Massachusetts Institute of Technology, Cambridge, MA, 1984.

[14] P. H. Meckl. *Control of Vibration in Mechanical Systems Using Shaped Reference Inputs*. PhD thesis, Massachusetts Institute of Technology, Cambridge, MA, 1988.

[15] A. K. M. Azad, M. H. Shaheed, Z. Mohamed, M. O. Tokhi, and H. Poerwanto. Open-Loop Control of Flexible Manipulators Using Command-Generation Techniques. In M. O. Tokhi and A. K. M. Azad, editors, *Flexible Robot Manipulators: Modelling, Simulation and Control*, pages 207–234. Institution of Engineering and Technology, London, UK, 2008.

[16] D. D Roover and F. B. Sperling. Point-to-point Control of a High Accuracy Positioning Mechanism. In *Proceedings of the American Control Conference*, pages 1350–1354, Albuquerque, NM, 1997.

[17] V. M. Beazel and P. H. Meckl. Command Shaping Applied to Nonlinear Systems with Configuration-Dependent Resonance. In *Proceedings of the 2005 American Control Conference*, pages 539–544, 2005.

[18] L. Y. Pao and M. A. Lau. Robust input shaper control design for parameter variations in flexible structures. *Journal of dynamic systems, measurement, and control*, 122(1):63–70, 2000.

[19] W. Chatlatanagulchai, V. M. Beazel, and P. H. Meckl. Command Shaping Applied to a Flexible Robot with Configuration-Dependent Resonance. In *Proceedings of the 2006 American Control Conference*, pages 1766–1771, Minneapolis, MN, 2006.

[20] V. M. Beazel. *Command Shaping Applied to Nonlinear Systems with Configuration-Dependent Resonance*. PhD thesis, Purdue University, West Lafayette, IN, 2004.

[21] J. Yegerlehner. *The Application of Artificial Neural Networks to the Control of Nonlinear System Undergoing Changes in a System Parameter*. Master's thesis, Purdue University, West Lafayette, IN, 1992.

[22] R. Kinceler. *Manipulator Manual: To Configure from Flexible Joints to Rigid Joints and Vice-Versa*. Purdue University, 1996.

[23] W. Chatlatanagulchai. *Backstepping Intelligent Control Applied to a Flexible-Joint Robot Manipulator*. PhD thesis, Purdue University, West Lafayette, IN, 2006.

[24] H. C. Nho. *Precise Motion Control of Flexible-Joint Robot Manipulators with an Intelligent Payload Estimator*. PhD thesis, Purdue University, West Lafayette, IN, 2004.

[25] M. Spong. Modeling and Control of Elastic Joint Robots. *J Dyn Syst-T ASME*, 109:310–319, 1987.

[26] R. S. Lee. *Optimal Parameter Estimation for Long-Term Prediction in the Presence of Model Mismatch Applied to a Two-Link Flexible-Joint Robot*. PhD thesis, Purdue University, West Lafayette, IN, 2011.

[27] A. Scheel. *System Identification of Two-link Flexible Joint Robot*, 2011. `http://engineering.purdue.edu/~sysIDreport`.

[28] A. Ghosal. *Robotics: Fundamental Concepts and Analysis*. Oxford University Press, 2006.

[29] D. M. Aspinwall. Acceleration Profiles for Minimizing Residual Response. *J Dyn Syst-T ASME*, 102:3–6, 1980.

[30] R. Bellman, I. Glicksberg, and O. Gross. *On the "bang-bang" Control Problem*. Rand Corporation, 1955.

[31] J. P. LaSalle. Time optimal control systems. *Proceedings of the National Academy of Sciences of the United States of America*, 45(4):573, 1959.

[32] K. Raeen. *A Study of The Gibbs Phenomenon in Fourier Series and Wavelets*. Master's thesis, The University of New Mexico, 2005.

[33] S. E. Kelly. Gibbs phenomenon for wavelets. *Applied and Computational Harmonic Analysis*, 3(1):72–81, 1996.